

**$T_1$  Anisotropy Elucidates Spin Relaxation Mechanisms in an  $S = 1$  Cr(IV)  
Optically Addressable Molecular Qubit**

Nathanael P. Kazmierczak<sup>†</sup>, Kaitlin M. Luedecke<sup>†</sup>, Elisabeth T. Gallmeier, and Ryan G. Hadt\*

Division of Chemistry and Chemical Engineering, Arthur Amos Noyes Laboratory of Chemical  
Physics, California Institute of Technology, Pasadena, California 91125, United States

<sup>†</sup>Co-first authors

\*Corresponding author: [rghadt@caltech.edu](mailto:rghadt@caltech.edu)

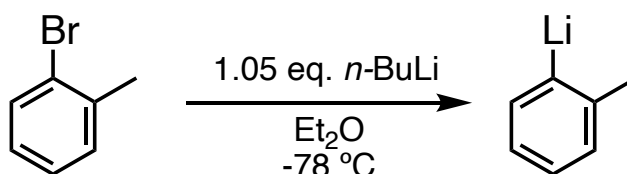
## Table of Contents

<b>1. General Considerations .....</b>	<b>3</b>
1.1 Materials and Synthesis.....	3
( <i>o</i> -tolyl)lithium (Li( <i>o</i> -tolyl)): .....	3
Tetrakis( <i>o</i> -tolyl)chromium(IV) (Cr( <i>o</i> -tolyl) <sub>4</sub> ):.....	4
1.2 Solid State Dilutions for EPR Analysis.....	4
1.8% Cr( <i>o</i> -tolyl) <sub>4</sub> in Sn( <i>o</i> -tolyl) <sub>4</sub> : .....	4
2.2% Cr( <i>o</i> -tolyl) <sub>4</sub> in Sn( <i>o</i> -tolyl) <sub>4</sub> (co-crystallized):.....	4
0.1% Cu(acac) <sub>2</sub> in Pd(acac) <sub>2</sub> : .....	4
<b>2. Experimental Methods.....</b>	<b>4</b>
2.1 Continuous Wave Electron Paramagnetic Resonance .....	4
2.2 Pulsed Electron Paramagnetic Resonance.....	7
<b>3. Echo Detected Field Sweeps .....</b>	<b>8</b>
<b>4. Experimental Determination of the Sign of ZFS in Cr(<i>o</i>-tolyl)<sub>4</sub>.....</b>	<b>9</b>
<b>5. <math>T_1</math> Anisotropy Plots.....</b>	<b>16</b>
5.1 Workflow for Building $T_1$ Anisotropy Plots .....	16
5.2 Additional $T_1$ Anisotropy Experiments .....	17
5.3 Supplemental Discussion of $T_1$ Anisotropy Fitting Functions .....	20
<b>6. Theoretical Derivation of <math>T_1</math> Anisotropy Functional Forms .....</b>	<b>28</b>
6.1 $S = \frac{1}{2}$ rotational mode $T_1$ anisotropy.....	28
6.2 $S = 1$ rotational mode $T_1$ anisotropy.....	29
<b>7. Tabulated <math>T_1</math> Values .....</b>	<b>32</b>
<b>References .....</b>	<b>35</b>

# 1. General Considerations

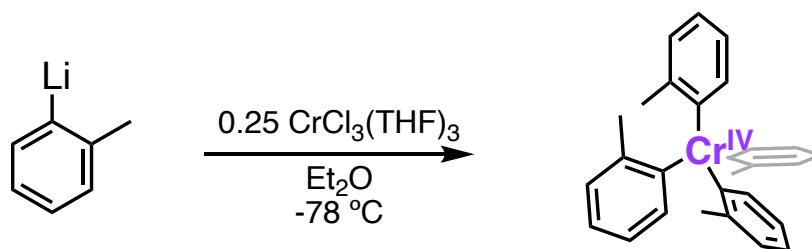
## 1.1 Materials and Synthesis

Air-free syntheses were conducted using Schlenk technique under dinitrogen atmosphere with glassware that was either oven-dried at 150 °C overnight or for at least 1 hour after flame drying. Diethyl ether (Et<sub>2</sub>O), hexanes, and tetrahydrofuran (THF) were dried using a Pure Process Technology solvent purification system and stored over activated 3 Å molecular sieves for at least 1 night prior to use. Hexamethyldisiloxane (HMDSO, Sigma-Aldrich, ≥ 98%) was refluxed over calcium hydride at 60 °C for 2 hours, distilled, subjected to 3 freeze-pump-thaw cycles, and then stored over 3 Å molecular sieves for at least 1 night prior to use. 2-bromotoluene (MilliporeSigma, 99%) was subjected to 3 freeze-pump-thaw cycles and then stored over 3 Å molecular sieves for at least 1 night prior to use to remove dissolved gases and water content. *N*-butyllithium (*n*-BuLi, Sigma-Aldrich, 2.5 M in hexanes), chromium(III) chloride tetrahydrofuran complex (1:3) (CrCl<sub>3</sub>(THF)<sub>3</sub>, Acros Organics, 98%), tetrakis(*o*-tolyl)tin(IV) (Sn(*o*-tolyl)<sub>4</sub>, Sigma-Aldrich), copper (II) acetylacetonate (Cu(acac)<sub>2</sub>, Sigma-Aldrich, ≥ 99.9% trace metal basis), and palladium(II) acetylacetonate (Pd(acac)<sub>2</sub>, Sigma-Aldrich, 99%) were used without further purification. For non-air-free syntheses/workups, solvents used were either ACS or reagent grade.



**Scheme S1.** Synthesis of Li(*o*-tolyl).

**(*o*-tolyl)lithium (Li(*o*-tolyl)):** (*o*-tolyl)lithium was prepared according to a modified literature procedure.<sup>1</sup> 20 mL of dry Et<sub>2</sub>O was added to a Schlenk flask containing 2-bromotoluene (3 g, 17.5 mmol) at -78 °C. After 10 minutes, 7.38 mL of *n*-BuLi (2.5 M in hexanes, 18.45 mmol) was slowly added to the reaction mixture, which was then stirred at -78 °C for an additional 30 minutes. The cold bath was then removed, and the reaction was allowed to warm to room temperature over the course of 1.5 hours. Volatiles were removed en vacuo, and the remaining yellow residue was washed with 2 x 20 mL of dry hexanes. The resulting white powder was then dried under vacuum, giving (*o*-tolyl)lithium in approximately quantitative yield.



**Scheme S2.** Synthesis of  $\text{Cr}(o\text{-tolyl})_4$ .

**Tetrakis(*o*-tolyl)chromium(IV) ( $\text{Cr}(o\text{-tolyl})_4$ ):**  $\text{Cr}(o\text{-tolyl})_4$  was prepared according to a modified literature report.<sup>2</sup> A Schlenk flask was charged with  $\text{Li}(o\text{-tolyl})$  (500 mg, 5.1 mmol) and 5 mL  $\text{Et}_2\text{O}$ . To another Schlenk flask,  $\text{CrCl}_3(\text{THF})_3$  (472.1 mg, 1.26 mmol) was added alongside 10 mL  $\text{Et}_2\text{O}$ . Both flasks were allowed to cool to  $-78^\circ\text{C}$ . After  $\sim 10$  minutes, the solution containing the aryl lithium reagent was transferred dropwise to the flask containing  $\text{CrCl}_3(\text{THF})_3$  solution. Once transfer was complete, the reaction flask was allowed to stir cold for 1.5 hours in the dark. The reaction was then allowed to warm to room temperature over the course of 30 minutes before volatiles were removed *en vacuo*. The reaction flask was then taken into the glovebox, where the purple/brown residue was taken up in  $\sim 20$  mL HMDSO and  $\sim 40$  mL hexanes, filtered through celite, and pumped dry. The residue was then successively washed with hexanes, filtered through celite, and pumped down until there remained no visible brown impurities. The resulting  $\text{Cr}(o\text{-tolyl})_4$  residue was isolated as a royal purple solid in  $\sim 10\%$  yield with UV-vis and EPR consistent with prior literature reports.<sup>3,4</sup>

## 1.2 Solid State Dilutions for EPR Analysis

**1.8%  $\text{Cr}(o\text{-tolyl})_4$  in  $\text{Sn}(o\text{-tolyl})_4$ :** In the glovebox, 2 mg of  $\text{Cr}(o\text{-tolyl})_4$  was dissolved in 15 mL of  $\text{Et}_2\text{O}$ . This solution was transferred to a vial containing 108 mg of  $\text{Sn}(o\text{-tolyl})_4$ . The solution was thoroughly mixed with a pipette until all the tin complex appeared dissolved. The solvent was then quickly evacuated to give the solid state dilution as a bright purple, crystalline powder.

**2.2%  $\text{Cr}(o\text{-tolyl})_4$  in  $\text{Sn}(o\text{-tolyl})_4$  (co-crystallized):** In the glovebox, 2.4 mg of  $\text{Cr}(o\text{-tolyl})_4$  was dissolved in 15 mL of  $\text{Et}_2\text{O}$ . This solution was transferred to a vial containing 108 mg of  $\text{Sn}(o\text{-tolyl})_4$ . The solution was thoroughly mixed with a pipette until all the tin complex appeared dissolved. The solution was then concentrated to  $\sim 5$  mL, and 10 mL hexanes were layered on top. The mixture was stored at  $-35^\circ\text{C}$  and gave bright purple crystals after  $\sim 1$  week. The crystals were then isolated from the supernatant, dried, ground via mortar and pestle, and used for EPR analysis.

**0.1%  $\text{Cu}(\text{acac})_2$  in  $\text{Pd}(\text{acac})_2$ :** This solid state dilution was prepared according to a previous literature report.<sup>5</sup> Briefly, 0.16 mg  $\text{Cu}(\text{acac})_2$  (diluted) and 203 mg  $\text{Pd}(\text{acac})_2$  were dissolved in  $\text{CHCl}_3$ , filtered, and precipitated by rotary evaporator.

## 2. Experimental Methods

### 2.1 Continuous Wave Electron Paramagnetic Resonance

Continuous wave (CW) X-band electron paramagnetic resonance (EPR) spectra were obtained from a Bruker EMX CW-EPR spectrometer equipped with an ER-4116DM Dual Mode resonator operating in perpendicular mode or a ER-4119HS High Sensitivity resonator. Samples were prepared in Norell 4 mm standard EPR tubes. Unless otherwise noted, spectra were collected in perpendicular mode ( $\sim 9.6$  GHz) with a modulation amplitude of 4 G and at a power of 0.5 mW (26 dB). Sample cooling was achieved with an Oxford Instruments ESR-900 liquid helium flow cryostat equipped with an ITC-503 temperature controller to access temperatures from 5 K – 80 K (liquid helium) or with a vacuum-sealed liquid nitrogen immersion dewar to access 77 K. When needed, spectra were baseline corrected by fitting the sloping baseline to a first-degree polynomial. Spectra were simulated using the EasySpin simulation toolbox (version 5.2.33) with MATLAB (version 2020b or 2021b).<sup>6</sup> Note the zero-field splitting was found to be mildly dependent on temperature ( $\pm \sim 2\%$  over the range 7 K – 60 K), consistent with a previous report.<sup>3</sup> Where quantitative simulations of the spin Hamiltonian for pulsed EPR  $T_1$  anisotropy were required, we used the spin Hamiltonian parameters extracted from the CW EPR spectrum acquired at the same temperature.

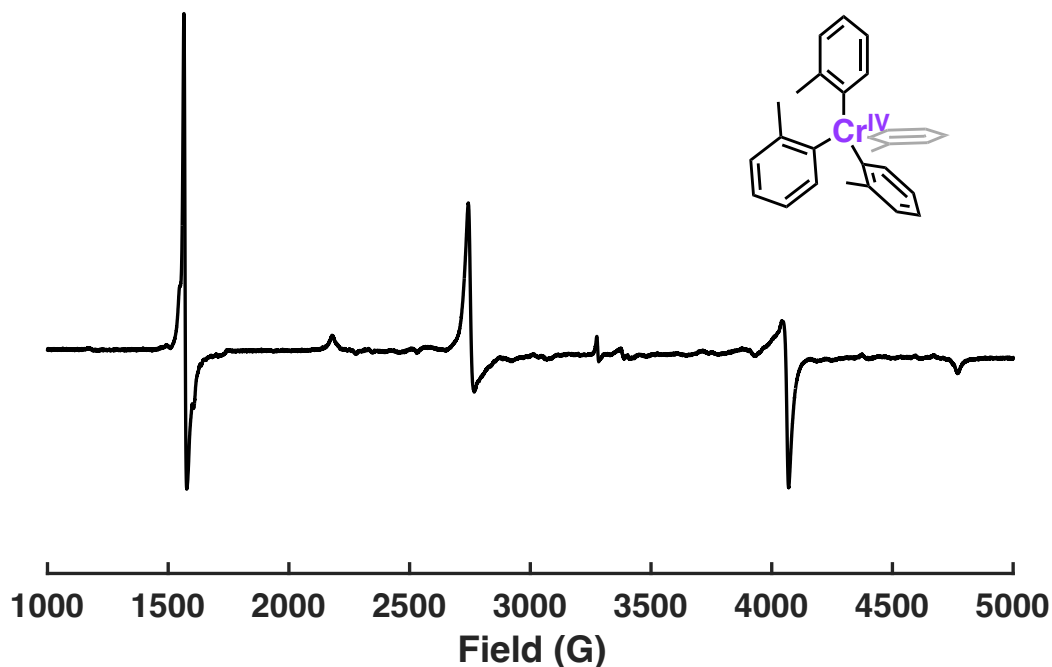


**Figure S1.** CW X-band EPR spectra collected for 1.8%  $\text{Cr}(\text{o-tolyl})_4$  in  $\text{Sn}(\text{o-tolyl})_4$  with an ER-4116DM Dual Mode resonator at 9.638 GHz and 0.5 mW power at 40 K. We note that the CW line broadening may arise from  $D$ -strain or unresolved hyperfine, consistent with a previous report for this compound.<sup>3</sup>

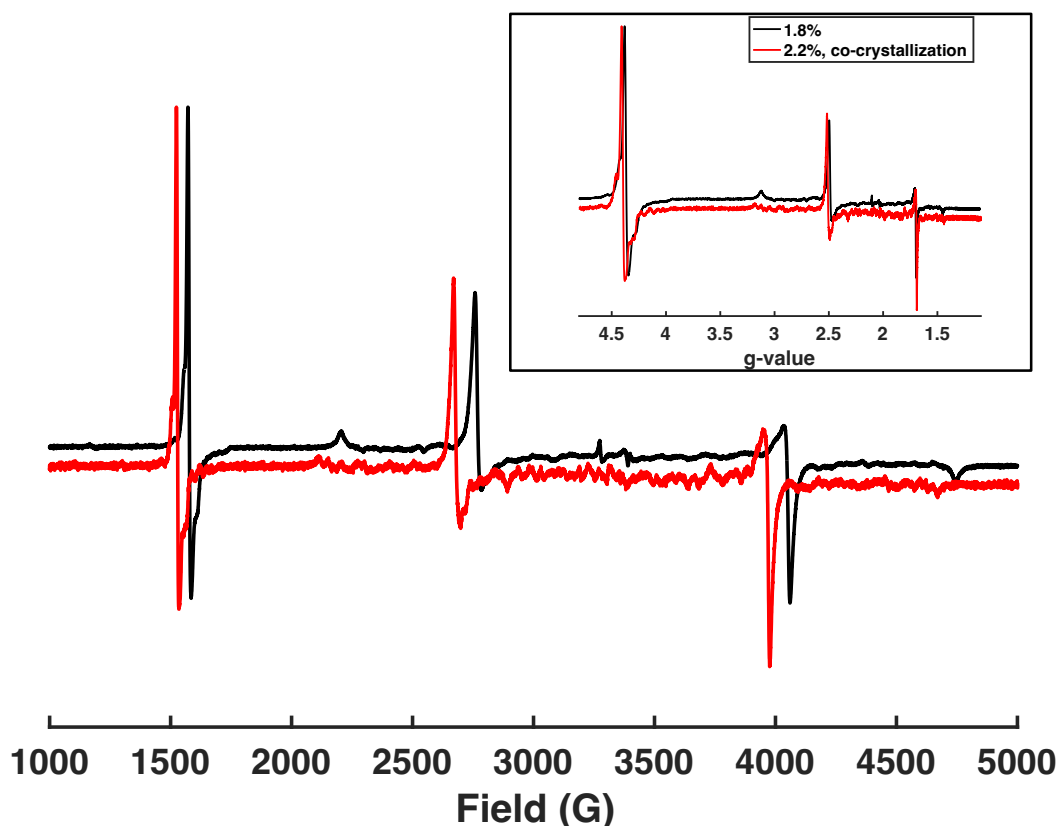


**Figure S2.** CW X-band EPR spectra collected for 1.8% Cr(*o*-tolyl)<sub>4</sub> (black line, collected with a ER-4116DM Dual Mode resonator at 9.638 GHz and 0.5 mW power) in Sn(*o*-tolyl)<sub>4</sub> and 2.2% co-crystallized Cr(*o*-tolyl)<sub>4</sub> in Sn(*o*-tolyl)<sub>4</sub> (red line, collected with a ER-4119HS High Sensitivity resonator at 9.405 GHz and 0.2 mW power) at 80 K, normalized to the maximum intensity of the half-field transition. *Inset:* spectra reported with respect to effective g value.

The samples used for the main  $T_1$  anisotropy experiments were prepared by fast evaporation of solvent. To ensure this did not introduce substantial disorder, additional samples were prepared by slow co-crystallization. The linewidths of the two sample preparations were compared by CW EPR (**Figure S2**) and found to be similar. Thus, fast precipitation does not introduce large amounts of aggregation or strain.

## 2.2 Pulsed Electron Paramagnetic Resonance

Pulsed X-band (~9.7 GHz) and Q-band (~34 GHz) EPR spectra were obtained from a Bruker ELEXSYS E580 pulsed EPR spectrometer equipped with a MD-4 resonator. Sample cooling was accomplished with an Oxford Instruments CF-935 liquid helium flow cryostat equipped with a Mercury temperature controller to access temperatures from 5 K – 100 K. Samples were prepared in Norell 4 mm standard EPR tubes for X-band measurements and in quartz capillary tubes for Q-band measurements. Echo-detected field sweeps (EDFS) were collected with a 2 pulse Hahn-echo sequence ( $\pi/2 - \tau - \pi - \tau - \text{echo}$ ). Inversion recovery experiments were collected with a  $\pi - t - \pi/2 - \tau - \pi - \tau - \text{echo}$ , where  $t$  is a variable time delay and  $\tau$  is a fixed constant that was optimized for each sample to maximize echo intensity. The video gain was optimized at each field position and temperature to maximize echo intensity for each sample as well. Four-step phase cycling was employed for inversion recovery measurements to eliminate secondary echoes and microwave ringdown. At X-band,  $\pi/2$  pulses were 8 ns long and  $\pi$  pulses were 16 ns long, and at Q-band,  $\pi/2$  pulses were 12 ns long and  $\pi$  pulses were 24 ns long unless otherwise noted. Picket fence saturation recovery experiments employed eight consecutive  $\pi/2$  pulses with a fixed interpulse delay of 1  $\mu\text{s}$ .

Inversion recovery and saturation recovery measurements were fit using a stretched exponential function in MATLAB (version 2020b or 2021b) (**Equation S1**). Error bars were extracted from the 95% confidence intervals on the fitted value of  $T_1$ .

$$I = Ae^{[-(\frac{t}{T_1})^\beta]} + I_0 \quad (\text{S1})$$

Hahn-echo decay measurements were fit using a stretched exponential function in MATLAB (version 2020b or 2021b) (**Equation S2**). Error bars were extracted from the 95% confidence intervals on the fitted value of  $T_m$ .

$$I = Ae^{[-(\frac{2t}{T_m})^\beta]} + I_0 \quad (\text{S2})$$

### 3. Echo Detected Field Sweeps

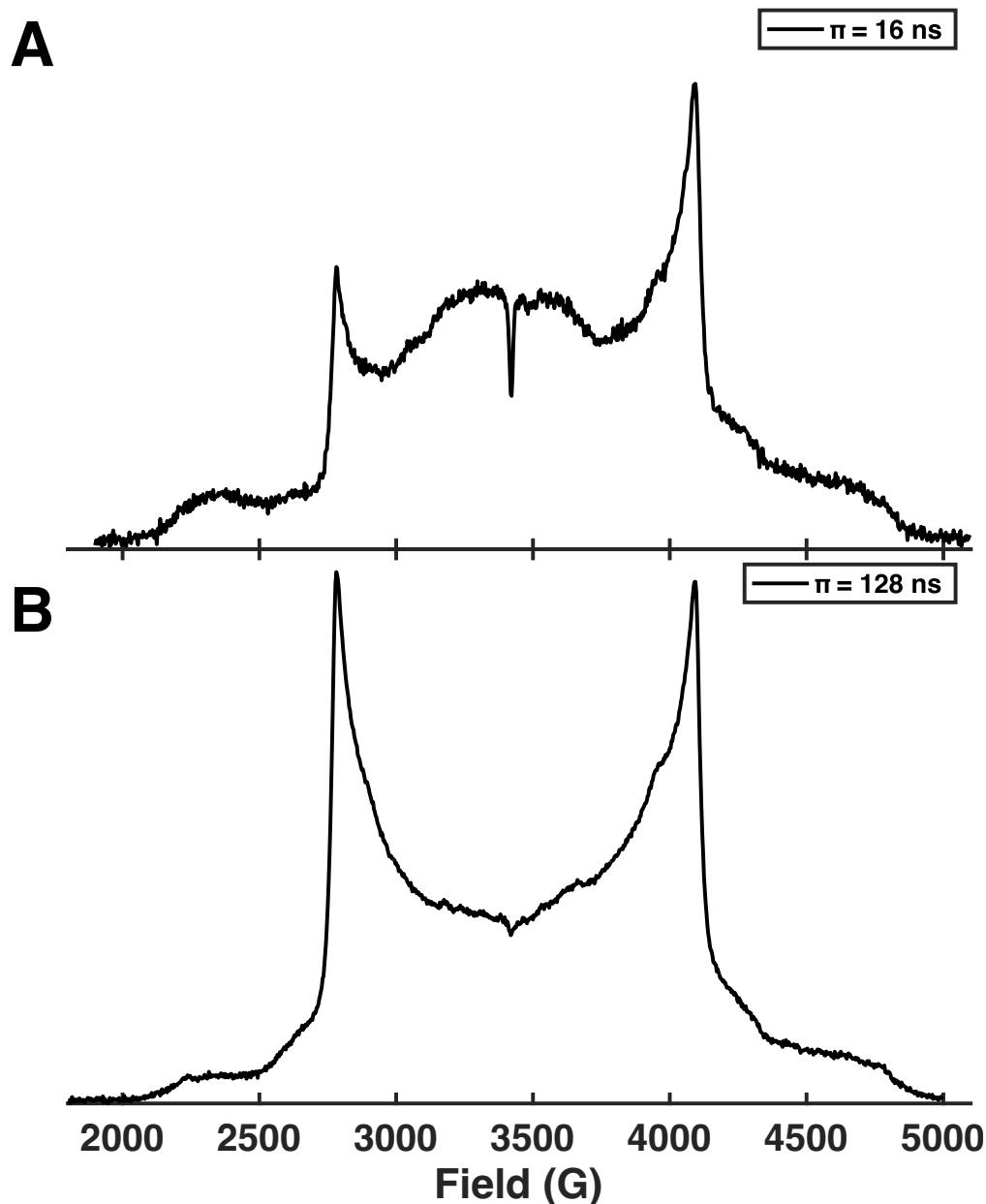


**Figure S3.** Comparison between X-band EPR spectra collected with hard ( $\pi = 16$  ns, **A**) vs. soft ( $\pi = 128$  ns, **B**) pulses for 2.2% Cr(*o*-tolyl)<sub>4</sub> in Sn(*o*-tolyl)<sub>4</sub> (co-crystallized) at 20 K. We note that the use of longer, soft pulses ( $\pi = 128$  ns) improves the spectral shape of the Pake pattern, particularly near  $\sim 2500$  G. We interpret differences between these spectra as ESEEM effects that are more prevalent when collecting with shorter, hard pulses ( $\pi = 16$  ns), owing to the greater bandwidth of  $\pi = 16$  ns exciting forbidden nuclear transitions required for ESEEM modulations.

X-band EDFs with hard ( $\pi = 16$  ns) pulses display deviations from the ideal simulated lineshape, including (a) asymmetric Pake pattern horns, and (b) an anomalous dip in the EDFs intensity at



3420 G (**Figure S3A**).  $T_m$  decay traces acquired with  $\pi = 16$  ns pulses show large ESEEM modulations and a consequent large field dependence of the fitted  $T_m$  values (**Figure S4**). Since a short period of echo decay is present in the EDFS pulse sequence, ESEEM and field-dependent  $T_m$  can affect the intensities and lineshapes in the EDFS spectra. Using softer pulses helps remove the ESEEM artifacts from the EDFS, leading to a symmetric Pake pattern very close to the ideal lineshape (**Figure S3B**). This indicates that the asymmetric lineshapes in **A** are due to ESEEM and not impurities. The anomalous central dip at 3420 G is mostly, but not completely, removed by the soft pulses. This may indicate that this feature is associated with excitation of forbidden transitions involving both  $M_s$  transitions, which become degenerate at the center of the EDFS for a given molecular orientation. This may speed cross relaxation<sup>7</sup>, accounting for the reduced EDFS intensity and faster spin-lattice relaxation observed at this field position. Similar anomalous features have been observed previously in Cr(IV) EPR and attributed to either a magnetically concentrated species or a double-quantum transition, which has been observed in  $S = 1$  anionic NV<sup>-</sup> centers as well.<sup>3,8,9</sup> Regardless of the precise origin of this feature, it is a localized outlier that does not affect the behavior of the rest of the spectrum. We therefore remove this field from consideration of  $T_1$  anisotropy in the fits reported in the main text (**Figure 2B**).

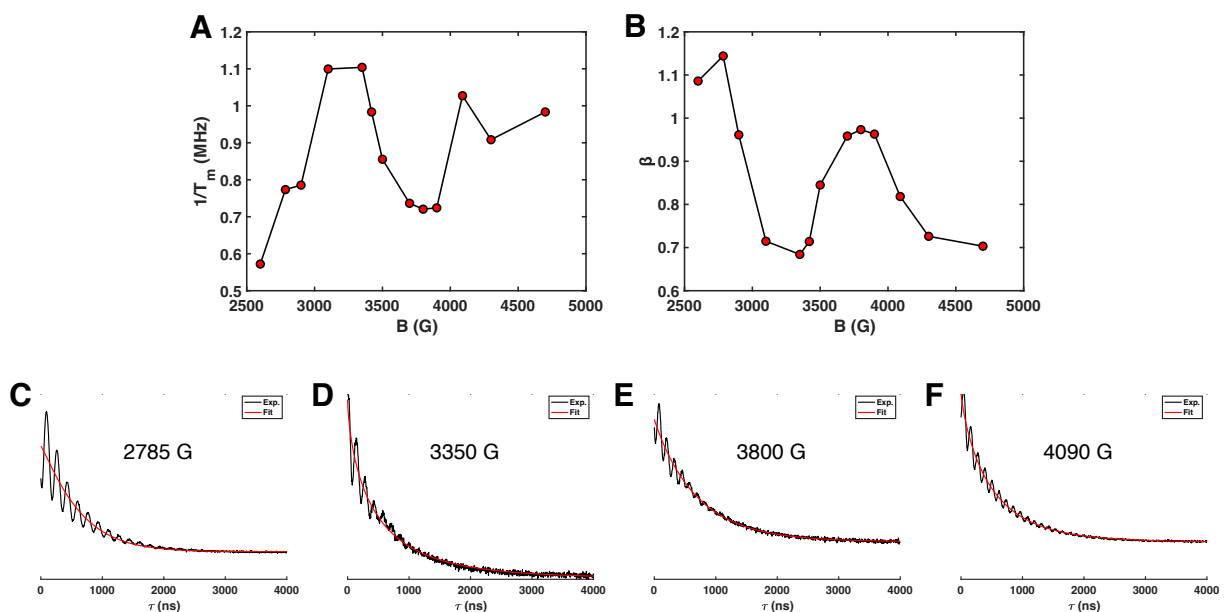


**Figure S4.** X-band  $T_m$  anisotropy plot for 2.2% Cr(*o*-tolyl)<sub>4</sub> in Sn(*o*-tolyl)<sub>4</sub> collected with  $\pi = 16$  ns pulses at 20 K. We note that on the whole, there is not a substantial anisotropy match between  $1/T_m$  or the stretching factors ( $\beta$ ) (**A**, **B**) and the  $T_1$  anisotropy at 40 K (**Figure 2B** in main text). We also note substantial ESEEM oscillations in the decay traces (**C-F**).

#### 4. Experimental Determination of the Sign of ZFS in Cr(*o*-tolyl)<sub>4</sub>

The sign of the axial zero-field splitting (ZFS) parameter,  $D$ , is an important consideration when constructing the energy level diagram of tetraaryl chromium(IV) complexes. Computations have predicted the sign of  $D$  to be negative.<sup>10,11</sup> To the best of our knowledge, the sign of  $D$  has yet to

be determined experimentally. To do so, we utilized variable-temperature Q-band EPR. The intensity of an EPR transition is affected by the difference in Boltzmann populations between the two levels involved in the transition, and at low temperatures, the EPR spectrum will become selective for excitations out of the magnetic ground state. Since the field positions of the ground-state transitions change with the sign of  $D$  (**Figures S5-S6**), variable-temperature EPR can in principle detect the sign of  $D$ , provided that the temperature is low enough to appreciably depopulate magnetic excited states. Q-band offers two advantages over X-band for this task: (1) the higher microwave frequency ( $\sim 34$  GHz vs.  $\sim 9.6$  GHz) results in a greater energetic splitting of the  $M_s$  sublevels and, thus, greater differential spin polarization from the Boltzmann distribution, and (2)  $^1\text{H}$  ESEEM modulations are greatly suppressed at Q-band, leading to pulsed EPR lineshapes closer to the ideal Pake pattern than at X-band. Ideal Pake pattern lineshapes are essential for accurate quantification of the relative populations in the two  $M_s$  transitions. We additionally employed soft pulses ( $\pi = 80$  ns) to further reduce ESEEM contributions.

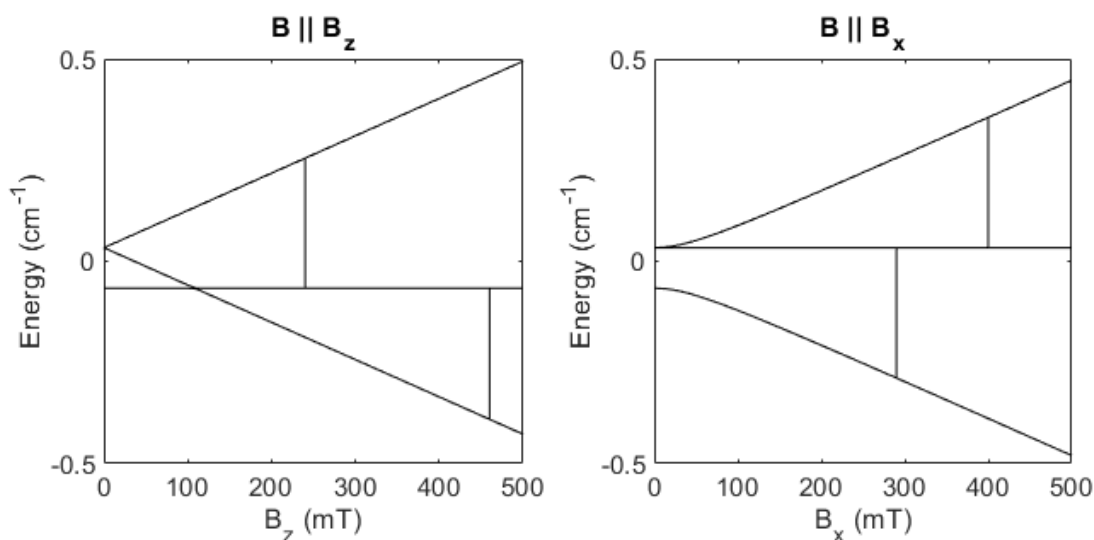


**Figure S5:** X-band energy level diagrams for an axial  $S = 1$  system with  $g = 1.98$  and  $D = +0.1$   $\text{cm}^{-1}$ . Vertical lines indicate the field positions where the microwave frequency (9.6 GHz) matches the sublevel energy gap. The rightmost parallel orientation transition corresponds to the ground state, while the leftmost perpendicular orientation transition is from the ground state.

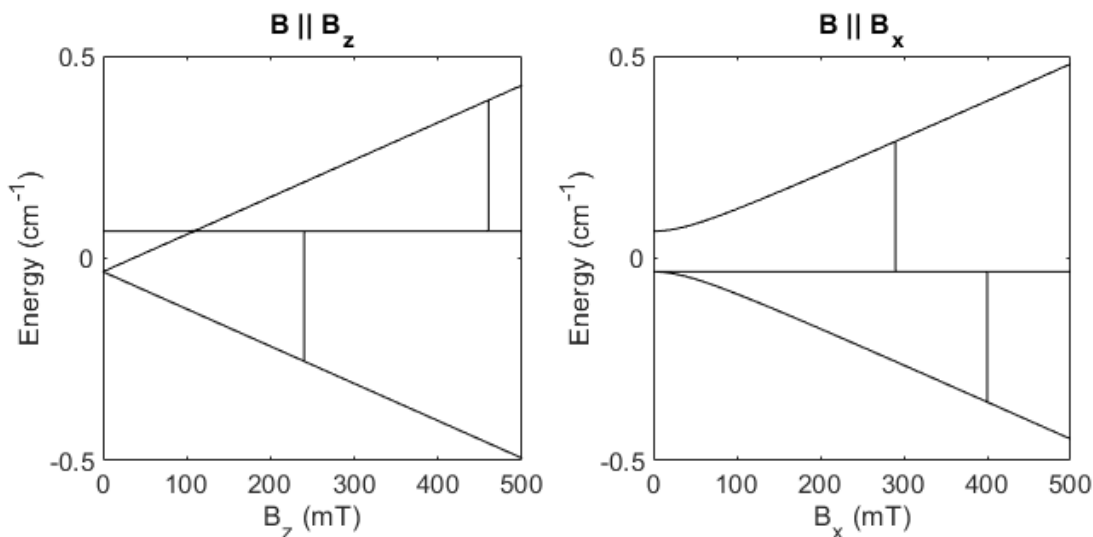


**Figure S6:** X-band energy level diagrams for an axial  $S = 1$  system with  $g = 1.98$  and  $D = -0.1$  cm<sup>-1</sup>. Vertical lines indicate the field positions where the microwave frequency (9.6 GHz) matches the sublevel energy gap. The leftmost parallel orientation transition corresponds to the ground state, while the rightmost perpendicular orientation transition is from the ground state.

EDFSs of Cr(*o*-tolyl)<sub>4</sub> collected at various temperatures were simulated using the EasySpin (version 5.2.33) with MATLAB (version 2020b or 2021b).<sup>6</sup> All spectra were normalized to the low-field perpendicular feature at  $\sim 1160$  mT. This normalization allowed for easy comparison of how the intensities of other features in the spectra change as a function of temperature. Specifically, we focused on the intensity of the high-field perpendicular feature centered at  $\sim 1290$  mT as a readout of the sign of  $D$  (**Figure S7**).

With  $+D$ , simulations indicate that as temperature increases, the intensity of the high-field perpendicular feature increases relative to a normalized low-field perpendicular feature. We also see an increase in intensity of the low-field parallel feature centered around  $\sim 1120$  mT. However, with  $-D$ , simulations indicate an opposite trend: the intensity of the low-field parallel feature and the high-field perpendicular feature decrease with increasing temperature when keeping the intensity of the low-field perpendicular feature fixed (**Figure S7**).

Q-band EDFs were then collected as a function of temperature and compared to the simulations. Upon comparison, we assign the sign of  $D$  as negative due to similarities in the spectral profile trends simulated for  $-D$  (**Figure S7**). In addition to following the same qualitative trend in decreasing intensity, the percent change in intensity of the high-field perpendicular feature also compares quite well with what is expected from simulation.

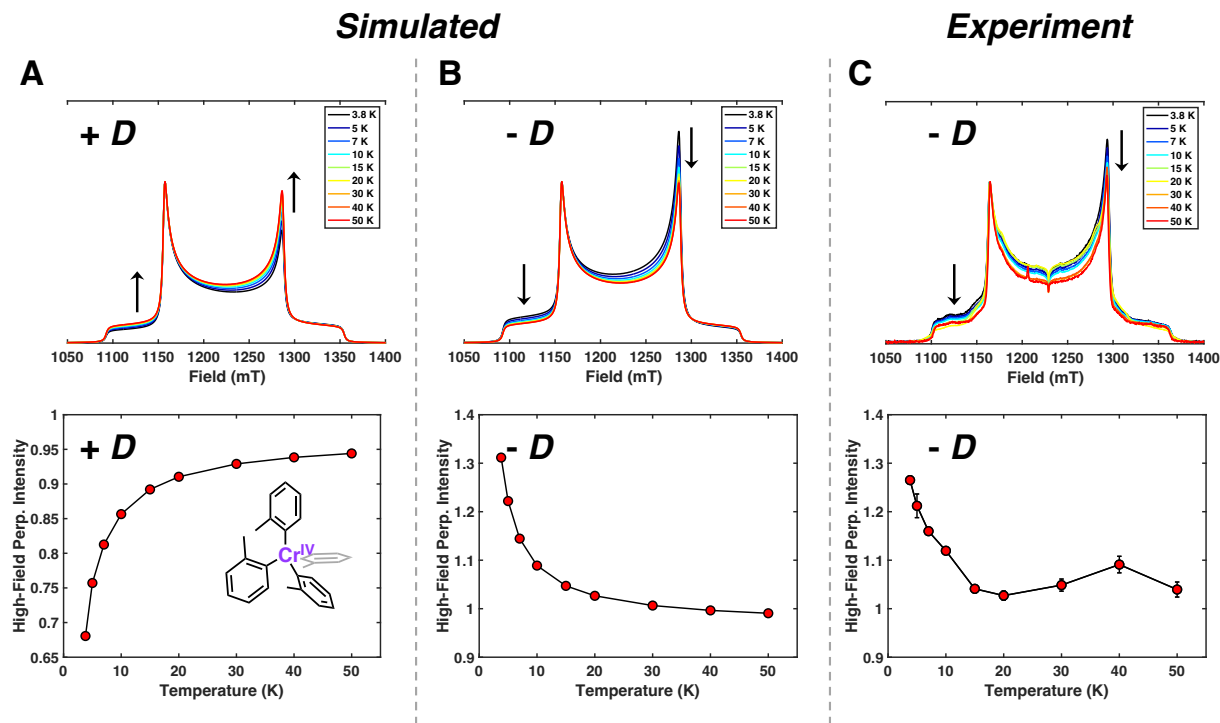


**Figure S7.** Determination of the sign of  $D$  for  $\text{Cr}(o\text{-tolyl})_4$ . Simulated EDFS for  $D > 0$  (A), simulated EDFS for  $D < 0$  (B), and experimental data for 1.8%  $\text{Cr}(o\text{-tolyl})_4$  in  $\text{Sn}(o\text{-tolyl})_4$  (C). The lower panels are read-outs of the intensity of the high-field perpendicular feature centered at  $\sim 1290$  mT with respect to a normalized low-field perpendicular feature. Soft pulses ( $\pi = 80$  ns) were employed.

For ease with the simulations, the magnitude of  $D$  was fixed at  $0.12 \text{ cm}^{-1}$ , which compared well with the experimental  $|D|$  in this temperature regime. Additionally, a Lorentzian linewidth of 4 mT (FWHM) was applied. The experimental sample was 1.8%  $\text{Cr}(o\text{-tolyl})_4$  in  $\text{Sn}(o\text{-tolyl})_4$ . Here, we are directly reading out the intensity of the maximum high-field perpendicular intensity after normalization of each spectrum to the maximum intensity of its low-field perpendicular peak. This method of analysis for the experimental determination of the sign of  $D$  differs from and complements what is presented in the main text using full-spectrum fits (*vide infra*). However, we note that regardless of whether we read-out intensity at one field position versus execute a full spectrum fit, we obtain the same result: the EDFS intensities agree well with the simulations for  $D < 0$ .

For a more rigorous analysis, as presented in the main text, that was not as sensitive to noise in the readout of intensities, we simulated the various  $M_S$  ( $-1 \rightarrow 0$ ;  $0 \rightarrow +1$ ) transitions in EasySpin using the Opt.Output = ‘separate’ option. The individual  $M_S$  transitions were then fit to the experimental EDFS spectrum, and the weighting coefficients on each transition were used to quantify their fractional contributions to the spectral intensity observed in the EDFS (see main text **Figure 1**). These weights follow the expected temperature dependence from differential Boltzmann population of the ground state sublevels.

To demonstrate that the temperature-dependent change in EDFS intensities arise from changing Boltzmann sublevel populations (and thus reflect the sign of  $D$ ), it is essential to show that the

intensity changes do not simply arise from a temperature-dependent  $T_m$  anisotropy. We therefore performed variable-temperature Q-band Hahn echo decay experiments at the parallel and perpendicular features analyzed for the zero-field splitting. ESEEM is almost completely removed from the Hahn echo decay at Q-band with  $\pi = 80$  ns pulses (**Figure S8**). In general, the  $T_m$  values do not change by more than 20% across the spectrum at any temperature considered (**Figure S9**).

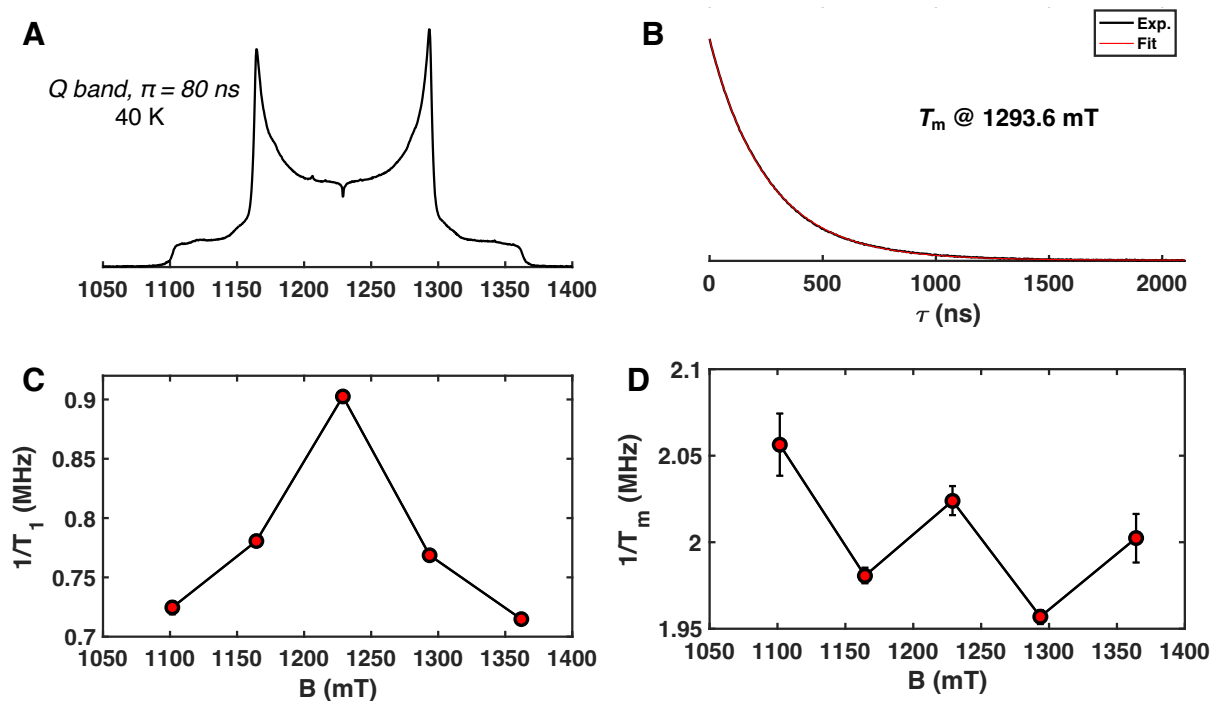


**Figure S8.** Pulsed Q-band EPR data for 1.8% Cr(*o*-tolyl)<sub>4</sub> in Sn(*o*-tolyl)<sub>4</sub> collected with  $\pi = 80$  ns pulses at 40 K. EDFS (**A**),  $T_m$  trace at 1293.6 mT (**B**),  $T_1$  anisotropy (**C**), and  $T_m$  anisotropy (**D**). We note substantially reduced ESEEM modulations in the decay traces at Q-band vs. X-band (**Figure S4**).

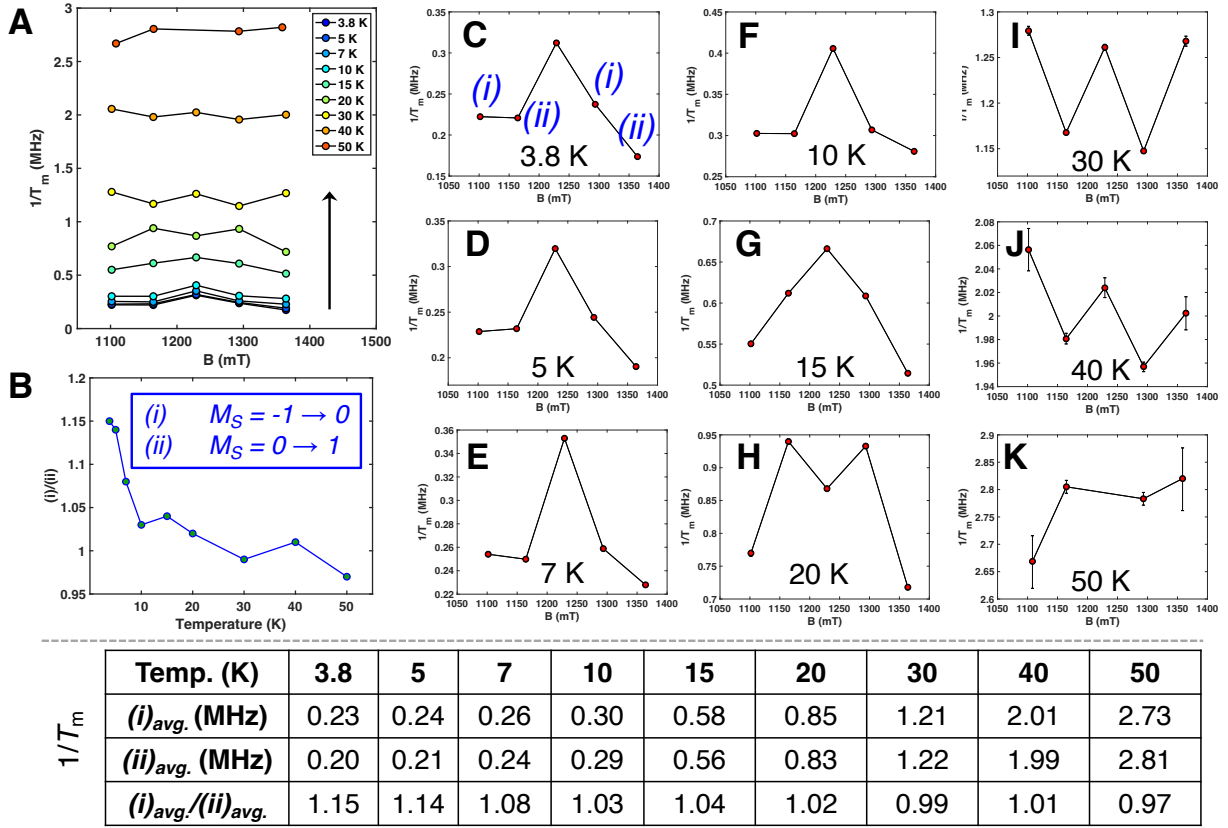


**Figure S9.** Q-band  $T_m$  anisotropy plots of 1.8% Cr(*o*-tolyl)<sub>4</sub> in Sn(*o*-tolyl)<sub>4</sub> collected with  $\pi = 80$  pulses. Overlaid  $1/T_m$  at various field positions, demonstrating that at higher temperatures, the rate of decoherence increases (A), average  $1/T_m$  of the transition (i) ( $M_S = -1 \rightarrow 0$ ) divided by  $1/T_m$  of transition (ii) ( $M_S = 0 \rightarrow +1$ ) (B), variable-temperature  $T_m$  anisotropy spanning from 3.8 K to 50 K (C-K), and tabulated values for  $1/T_m$  for various  $M_S$  transition.

For anisotropic  $T_m$  to cause the temperature-dependent intensity behavior in **Figure 1D**, it would be necessary that the echo decays be slower for the first transition (labeled (i) in **Figure 1**) relative to the second transition (labeled (ii) in **Figure 1**) at low temperatures but not at high temperatures. This behavior would lead to augmentation of the intensity of transition (i) over (ii) at low temperatures only, as observed experimentally in **Figure 1E**. However, examination of the temperature-dependent  $T_m$  values in **Figure S9** shows that, while there is some temperature-dependent  $T_m$  anisotropy, this cannot be the explanation for the changing EDFS intensities. Of the five fields at which  $T_m$  was measured, two correspond selectively to the (i) transition while two correspond selectively to the (ii) transition (**Figure S9C**). To quantify the relative echo decay rates, we averaged the two  $1/T_m$  for each manifold, and then examined the ratio of the average  $1/T_m$  for transition (i) vs. (ii). A ratio close to 1 indicates that  $T_m$  anisotropy does not bias towards EDFS intensity in either transition, while a ratio further from 1 indicates that  $T_m$  anisotropy alone could cause differential intensity changes between the two transitions.

There is a temperature-dependent change in the  $T_m$  ratio between the transitions (**Figure S9B**). However, this  $T_m$  anisotropy would tend to *reduce* the relative EDFS intensity of transition (i) at low temperatures, because the echo decays faster. In the experimental EDFS spectra, it is seen that

transition (i) has *increased* intensity at lower temperatures (**Figure 1D**). Thus, differential Boltzmann population and not anisotropic  $T_m$  leads to the intensity changes in **Figure 1D**, enabling our analysis to extract the sign of  $D$ . We have also attempted a correction for  $T_m$  anisotropy by simulating the predicted echo decay for transitions (i) and (ii) due to  $\tau = 300$  ns in the EDFS pulse sequence, assuming a monoexponential echo decay function (for  $T_m$  measured at Q-band here,  $\beta \approx 0.95$ ). Each intensity is divided by the simulated amount of decay over the Hahn echo period, removing the contribution of anisotropic  $T_m$  to the EDFS intensity. The resulting intensity ratios remain fully consistent with the expected intensity ratio on the basis of Boltzmann population effect (**Figure S10**).

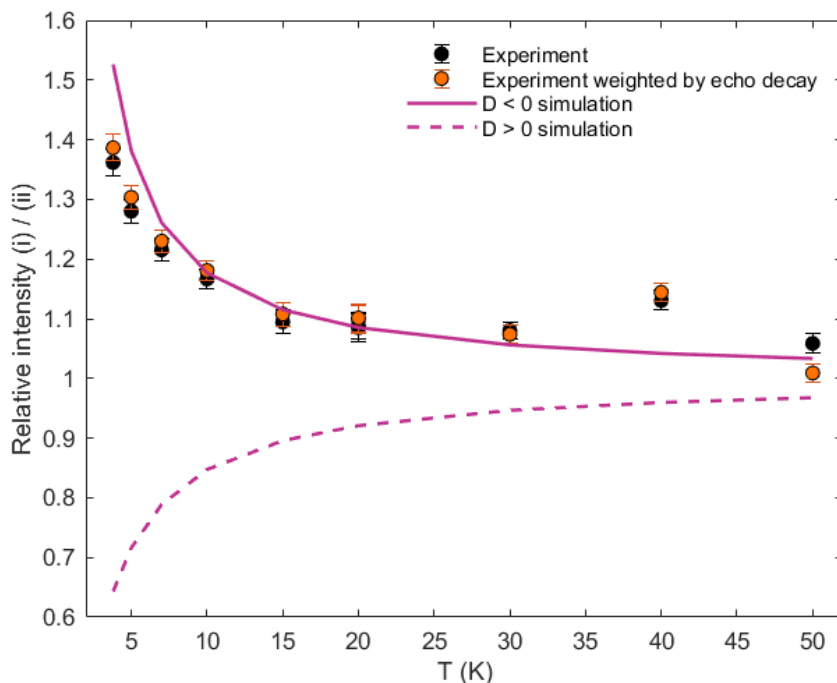


**Figure S10.** Quantification of variable temperature EDFS intensities for transitions (i) and (ii) including the correction for anisotropic  $T_m$ . Unweighted experimental data is the same as presented in **Figure 1E**.

## 5. $T_1$ Anisotropy Plots

### 5.1 Workflow for Building $T_1$ Anisotropy Plots

$T_1$  anisotropy is the concept that a studied system may have different spin-lattice relaxation, or  $T_1$ , values depending on the probed orientation, of the molecule. The field value  $B_0$  determines the probed orientation for a powder sample. Therefore, in order to probe  $T_1$  anisotropy and build a  $T_1$  anisotropy map, values of  $T_1$  must be obtained at given field positions. In practice, this analysis is achieved by first collecting an EDFS of the sample. Typically,  $\sim 30$ -50 specific field positions are chosen from which inversion recovery measurements will be made. Note that it is critical to choose field positions strategically so that not only the entire spectrum is well-described, but also so that the turning points on the spectra are collected as well. These points become especially important when understanding the orientation-dependence of  $T_1$ . Then, at each specified field position, an inversion recovery measurement is made. Each inversion recovery measurement is then fit to a stretched exponential function (**Equation S1**). Finally, the  $1/T_1$  values are plotted in MHz vs. the field they were collected at to achieve a  $T_1$  anisotropy map (**Figure S11**). The data contained in this plot can then be fit to various functional forms (see below) to extract important information about the modes that drive relaxation in the system.

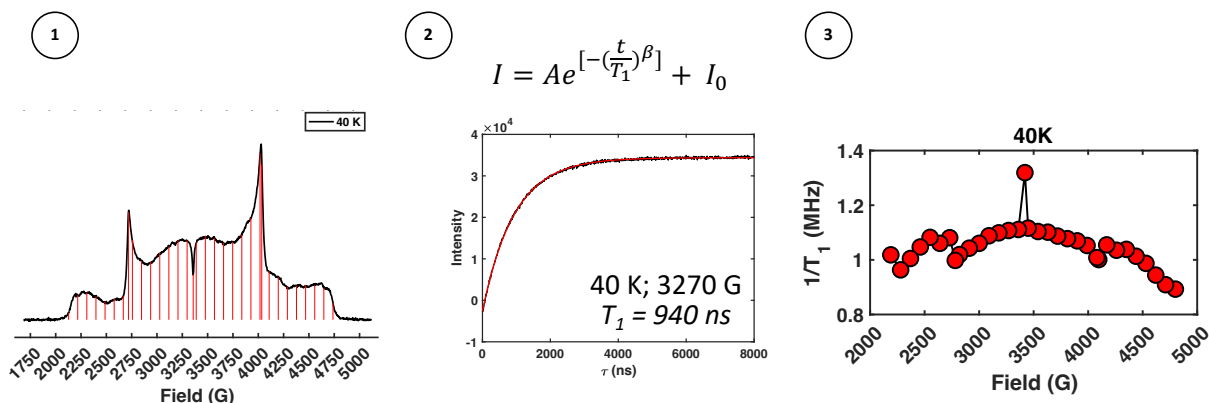


**Figure S11.** Workflow for building  $T_1$  anisotropy maps, shown for 1.8% Cr(*o*-tolyl) $_4$  in Sn(*o*-tolyl) $_4$  at 40 K. First, an EDFS is acquired, and field positions (shown as red lines) are identified for further data collection. Then, inversion recovery measurements are collected at specified field positions, and the data is fit to back-out  $T_1$  values. The rate of  $T_1$  relaxation ( $1/T_1$ ) is then plot versus field to realize a  $T_1$  anisotropy map.

The functional form contributions to the  $T_1$  anisotropy are extracted according to the following procedure, generalized from previous work on Cu(II) and V(IV)  $T_1$  anisotropy fitting.<sup>5</sup> Using the EasySpin<sup>6</sup> toolbox and Matlab R2020b, a uniformly dense grid of all possible molecular orientations relative to the magnetic field is constructed. The fields at which resonant microwave absorption occurs are acquired for each molecular orientation by simulation, using the spin Hamiltonian parameters extracted from the experimental CW EPR at the appropriate temperature. Next, the average molecular orientation  $\bar{\theta}$  is acquired by aggregating all orientations with a resonant field within a 5 G distance (Cr) or a 1 G distance (Cu) of a specified magnetic field value, and averaging  $\theta$  for each of these orientations. This process is repeated for each value of the magnetic field used in the field sweep measurement to build up a picture of how  $\bar{\theta}$  changes with  $B_0$ , as shown in **Figure 1C** in the main text. To compute  $\overline{\sin^2\theta}$  or  $\overline{\sin^2(2\theta)}$ , the identical grid is



used, and the values of  $\sin^2\theta$  or  $\sin^2(2\theta)$  for each orientation are averaged within the excitation bandwidth. The shapes of these functional forms are given in **Figures S18-S24**.

Once the simulated  $T_1$  anisotropy functions are generated, they can be fit to the experimental  $T_1$  anisotropy data via linear least-squares regression as previously described.<sup>5</sup> The coefficients on the linear least squares fit can then be used to quantify the amount of anisotropy arising from each individual functional form (for more details, see **Supporting Information Section 5.3**).

## 5.2 Additional $T_1$ Anisotropy Experiments

Several tests were employed to ensure the  $T_1$  anisotropy arises from a vibrational mechanism intrinsic to the molecule and not an artifact of the data processing. First, the stretched exponential fitting function was examined to ensure that the stretching factor did not vary greatly with field position, potentially introducing artifacts into the data fitting. For the  $\text{Cr}(o\text{-tolyl})_4$  inversion recovery measurements at 40 K, the stretching factors ( $\beta$ ) are very close to 1 ( $\sim 0.95$ ) and display minimal systematic changes with field position (**Figure S12A**). This indicates that the inversion recovery experiments are well described by pure exponentials. Indeed, fitting the 40 K  $T_1$  anisotropy with a monoexponential function yields a very similar  $T_1$  anisotropy pattern (**Figure S12B**). Thus, the choice of fitting function is not introducing artifacts into the  $T_1$  anisotropy.

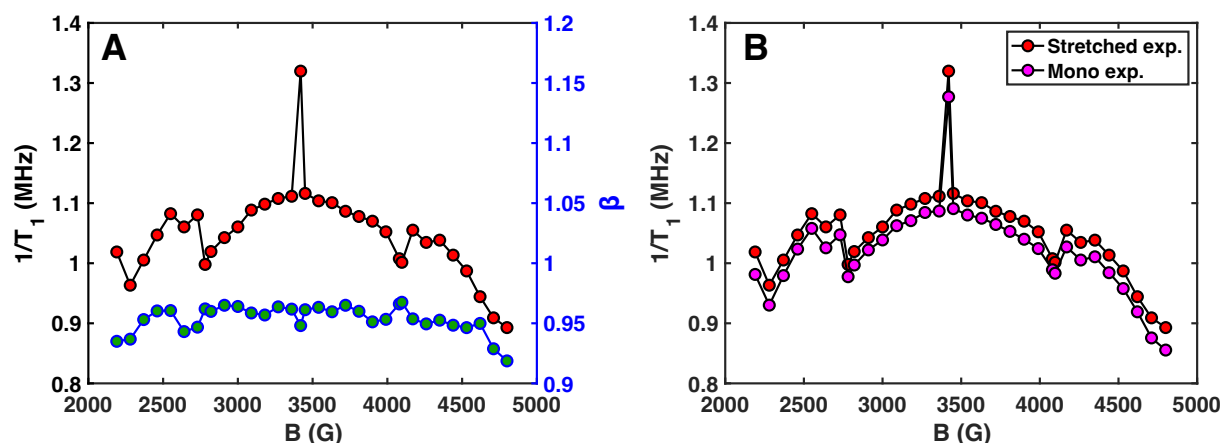


**Figure S12.**  $T_1$  anisotropy plots for 1.8%  $\text{Cr}(o\text{-tolyl})_4$  in  $\text{Sn}(o\text{-tolyl})_4$  collected with  $\pi = 16$  ns pulses at 40 K. We note that when  $T_1$  is fit with a stretched exponential, the anisotropy in the stretching factor ( $\beta$ ) is quite small (and that  $\beta$  itself is close to 1, a pure mono-exponential) and does not contribute to the anisotropy observed in  $T_1$  (A). This observation can be further visualized when comparing  $1/T_1$  fits with a stretched versus a mono-exponential factor (B).

It is additionally possible that spectral diffusion<sup>12</sup> could introduce artifacts into the measured  $T_1$  anisotropy if (a) spectral diffusion constitutes a major component of the observed inversion recovery, and (b) the spectral diffusion rate depends on the field position. Condition (a) is generally detectable by examining the stretching factor – when  $\beta \sim 1$ , spectral diffusion does not contribute, while if  $\beta \ll 1$ , spectral diffusion may account for much of the inversion recovery. For  $\text{Cr}(o\text{-tolyl})$

at 40 K, the observation that  $\beta = 0.95$  precludes anisotropic spectral diffusion as an explanation for the observed  $T_1$  anisotropy, and similarly for 60 K. For the 20 K and 7 K measurements, however,  $\beta$  deviates significantly further from 1, which could indicate spectral diffusion contributions (**Figure S13**). We therefore acquired  $T_1$  anisotropy measurements for  $\text{Cr}(o\text{-tolyl})_4$  at 7 K using a picket fence saturation recovery pulse sequence (**Figure S14A**), which can be more effective at removing spectral diffusion contributions to  $T_1$ .<sup>13</sup> While the measured  $1/T_1$  relaxation rates were indeed slower by saturation recovery by about 40%, consistent with the removal of some contributions to spin relaxation, the shape of the  $T_1$  is the same for both the inversion and saturation recovery experiments (**Figure S14B**). Thus, the  $T_1$  anisotropy in  $\text{Cr}(o\text{-tolyl})_4$  cannot be explained as merely arising from anisotropic spectral diffusion, pointing instead to an intrinsic vibrational mechanism. Similarly,  $\text{Cu}(\text{acac})_2$  displays large  $T_1$  anisotropy at temperatures (40 K and 100 K) where  $\beta$  is close to 1 (**Figure S13**), indicating that spectral diffusion is not responsible for the primary  $T_1$  anisotropy in  $\text{Cu}(\text{acac})_2$  either.

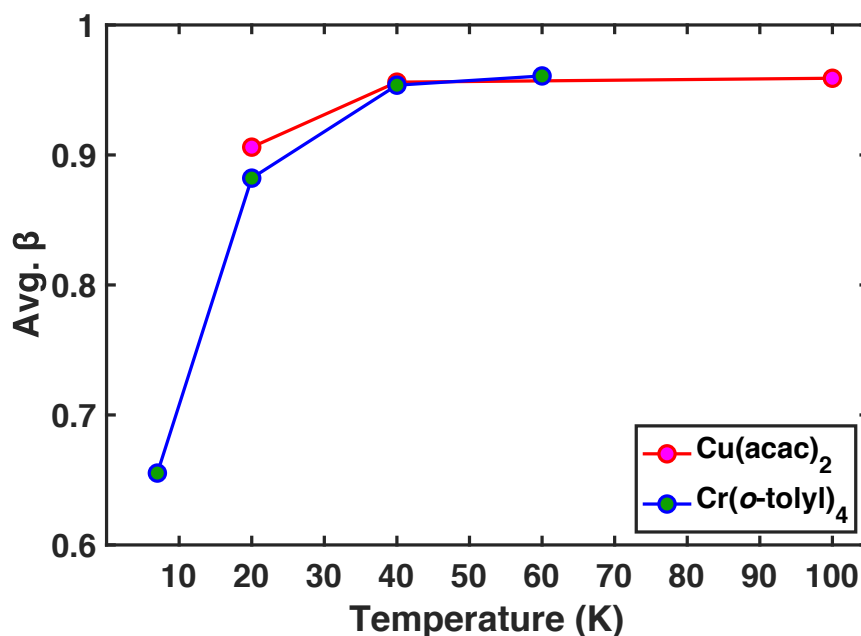


**Figure S13.** Temperature dependence of the average stretching factor ( $\beta$ ) obtained from stretched exponential fits to X-band inversion recovery data ( $\pi = 16$  ns pulses). Both 1.8%  $\text{Cr}(o\text{-tolyl})_4$  in  $\text{Sn}(o\text{-tolyl})_4$  and 0.1%  $\text{Cu}(\text{acac})_2$  in  $\text{Pd}(\text{acac})_2$  samples exhibit similar average stretching factor trends with temperature.

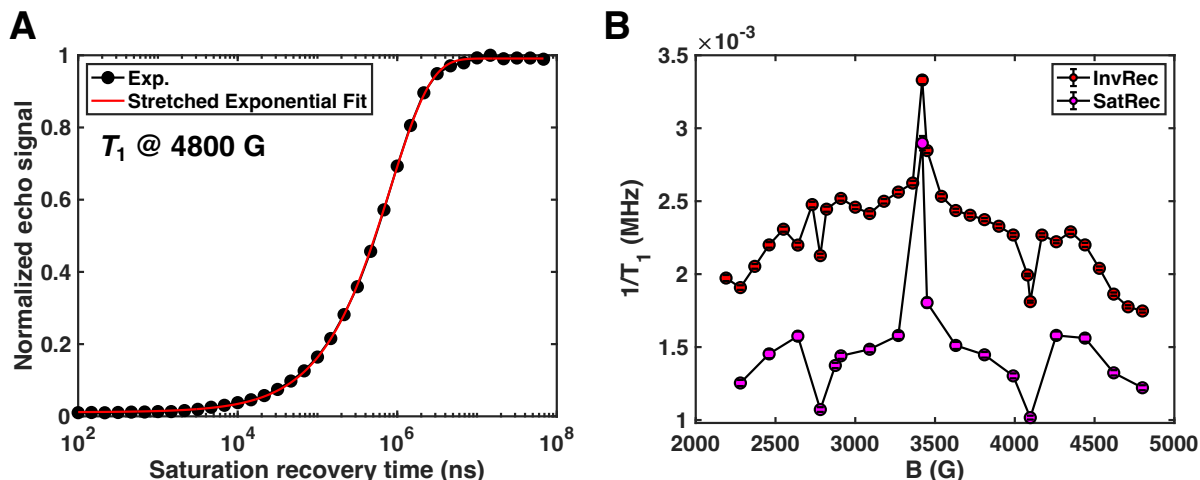


**Figure S14.** Comparison between saturation recovery and inversion recovery-obtained  $1/T_1$  for 1.8%  $\text{Cr}(o\text{-tolyl})_4$  in  $\text{Sn}(o\text{-tolyl})_4$  collected at 7 K. Saturation recovery measurement at 4800 G (A) and overlaid  $1/T_1$  anisotropy plots (B). Both methods were fit with stretched exponential forms.

Next, we examined the effect of pulse length on the measured  $T_1$ , as the X-band EDFS spectra change significantly for  $\pi = 128$  ns vs.  $\pi = 16$  ns pulses. Comparisons were made at 20 K instead of 40 K owing to the reduced signal-to-noise ratio of the  $\pi = 128$  ns experiments stemming from the smaller excitation bandwidth. The  $T_1$  anisotropy in both cases follows the same pattern (Figure S15), which at 20 K can be described as a 17.2%  $\sin^2(2\theta)$  and 6.2% of an inverted  $\sin^2(\theta)$  contribution (Table S2). Thus, the  $T_1$  anisotropy patterns with the  $\pi = 16$  ns pulses are fully reliably despite the influence of ESEEM on the lineshape of the EDFS (Figure S3).

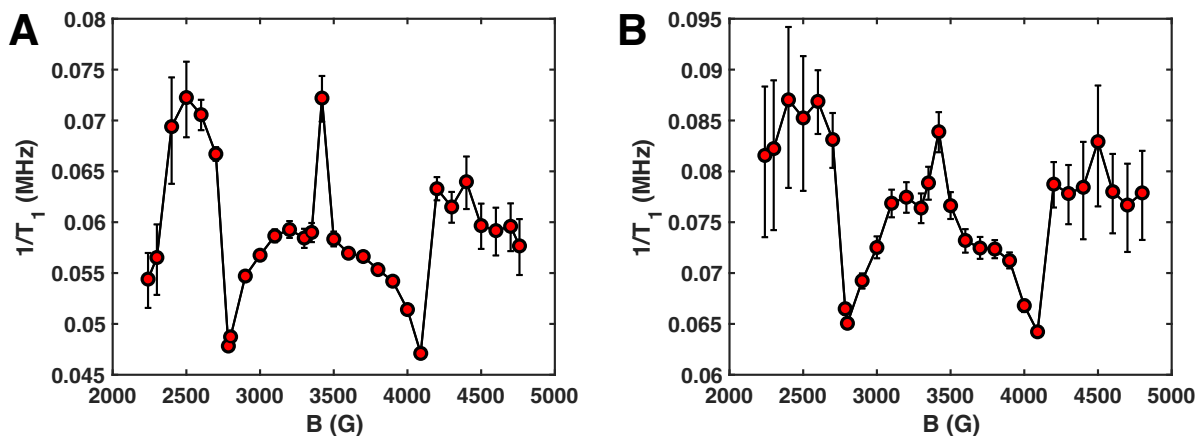


**Figure S15.**  $T_1$  anisotropy plots for 2.2%  $\text{Cr}(o\text{-tolyl})_4$  in  $\text{Sn}(o\text{-tolyl})_4$  with inversion recovery experiments collected with  $\pi = 16$  ns pulses (A) and  $\pi = 128$  ns pulses (B) at 20 K.

### 5.3 Supplemental Discussion of $T_1$ Anisotropy Fitting Functions

There exists a considerable amount of freedom in choosing how to define the anisotropy predictor functions for the  $1/T_1$  linear regression. All choices yield equal goodness of fit, but different values of the coefficients associated with each function; the goal is to maximize interpretability of the regression coefficients. First, to ensure the coefficients of the trigonometric functions were directly comparable to the linear function, the linear function was scaled to range from 0 to 1 over the range of the microwave absorption (see, for example, **Figure S16**). The  $\sin^2\theta$  and  $\sin^2(2\theta)$  naturally range between 0 and 1. The constant function was set at a value of 1 across the entire spectrum. All functions were defined to be strictly positive so that the total  $1/T_1$  can be described as the sum of additive contributions ascribable to physical mechanisms, since physical contributions to  $1/T_1$  cannot be negative. Thus, if linear regression yielded a negative coefficient on any function, that function was reflected around the line  $y = 0.5$ . Refitting then yields a positive coefficient that expresses the additive contribution to  $1/T_1$ . These conventions yield regression predictor functions exemplified by **Figure S16** for the case of  $\text{Cr}(o\text{-tolyl})_4$  anisotropy at 40 K. In accordance with these conventions, the regression functional form used for  $\sin^2\theta$  is inverted around  $y = 0.5$  for  $\text{Cr}(o\text{-tolyl})_4$  at 20 K as compared to 7 K, 40 K, and 60 K (**Figures S18-S21**).

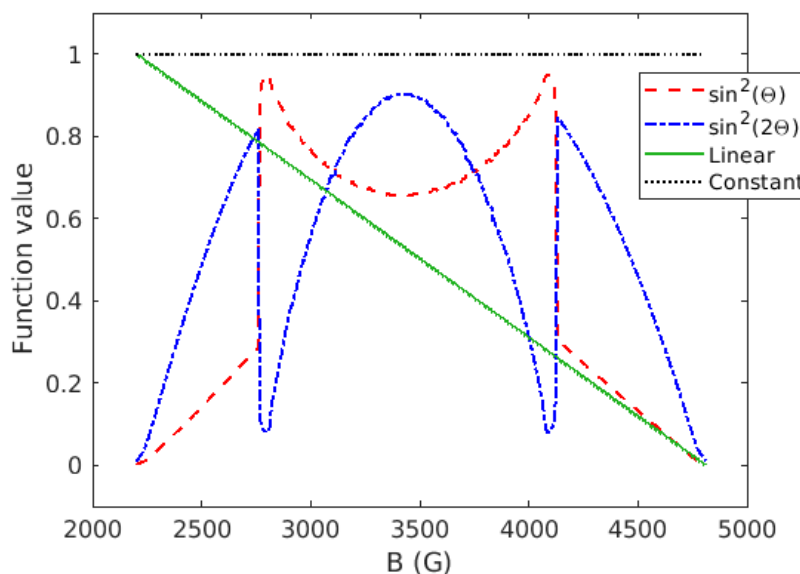


**Figure S16:** Predictor functions for the  $T_1$  anisotropy regression fit ( $\text{Cr}(o\text{-tolyl})_4$ , 40 K).

The contributions of each predictor function to the total fit are determined by multiplying the predictor by the regression coefficient. Since the anisotropy functions are defined to be strictly positive, the predictor contributions always add on top of each other to generate the total fit (**Figure S17**). The isotropic contribution to the  $T_1$  will generally be equal to the smallest value of  $1/T_1$  found at any field position. This baseline spin relaxation rate is shared by all orientations; hence, it is designated “isotropic”. The anisotropic contributions are comprised of the functional forms that must be stacked on top of the isotropic constant baseline to accurately simulate the data. Note that the linear contribution may be best thought of as a field-dependent isotropic contribution, as discussed in the main text. A field-dependent function for  $T_1$  could indicate either an effect of the molecular orientation (anisotropy) or simply that the magnitude of the magnetic field itself has a direct influence on the spin relaxation rate independent of orientation, as has been predicted via

the Debye model for the direct process.<sup>7</sup> True anisotropy functions should be a function of an orientation parameter ( $\theta$ ), but the linear function has no dependence on  $\theta$ , thereby indicating isotropic field dependence.

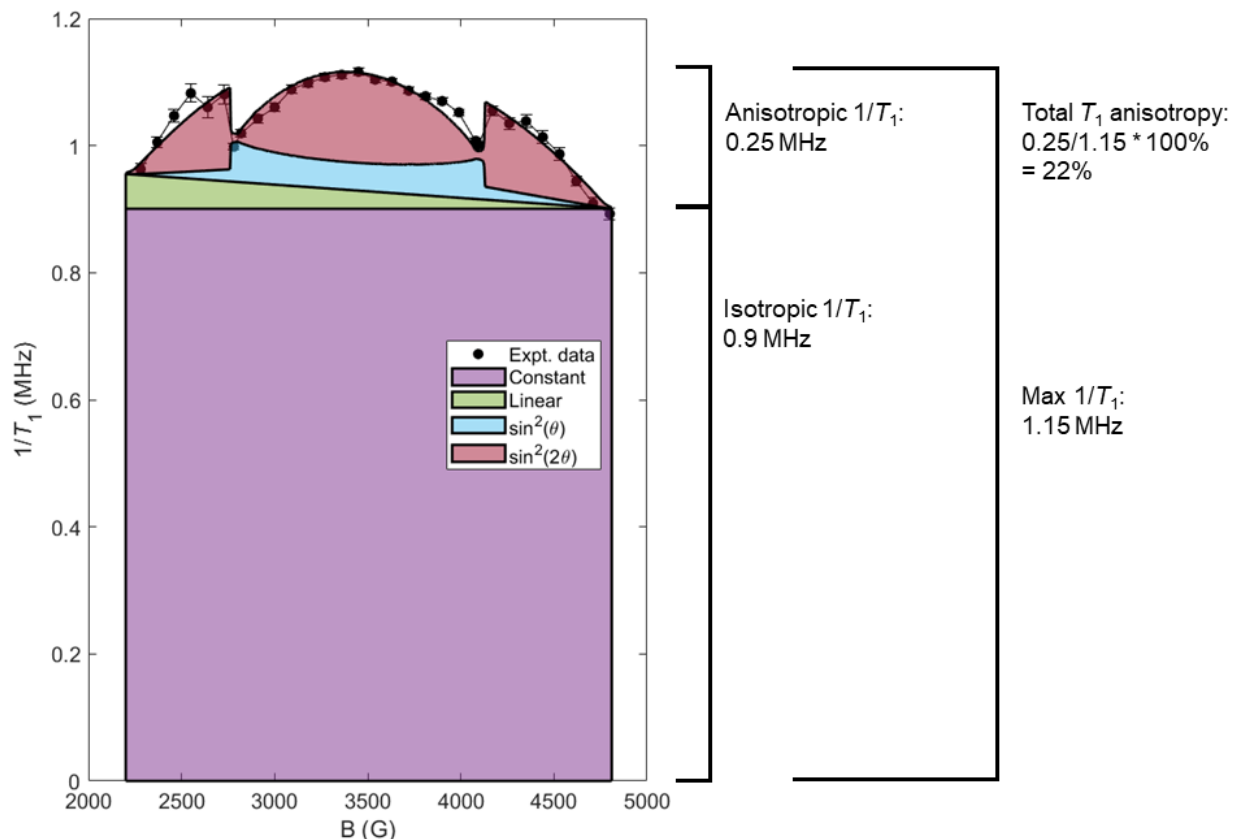


**Figure S17:** Additive contributions of the isotropic and anisotropic predictor functions towards simulating 40 K  $T_1$  anisotropy for  $\text{Cr}(o\text{-tolyl})_4$ .

In the following plots, the  $T_1$  simulations are graphically reported for  $\text{Cr}(o\text{-tolyl})_4$  and  $\text{Cu}(\text{acac})_2$  at all temperatures discussed in **Figure 3**. The unweighted predictor functions, weighted (but not vertically stacked) regression contributions, and total fit to the data are reported (**Figures S18 – S24**) along with a tabulation of the regression coefficients (**Tables S1-S2**). Note additionally that the anomalously fast relaxation times at the starred location in the EDFS spectra (**Figure 1D**) were deleted for each spectrum prior to fitting to the anisotropy functions. These outlier fast relaxation rates do not arise from  $T_1$  anisotropy, but probably reflect an enhanced cross-relaxation mechanism at the point where the two  $M_s$  transitions are exactly degenerate (*vide supra*). Including these points in the linear regression would bias the fits of the  $T_1$  anisotropy, and thus they are properly removed.

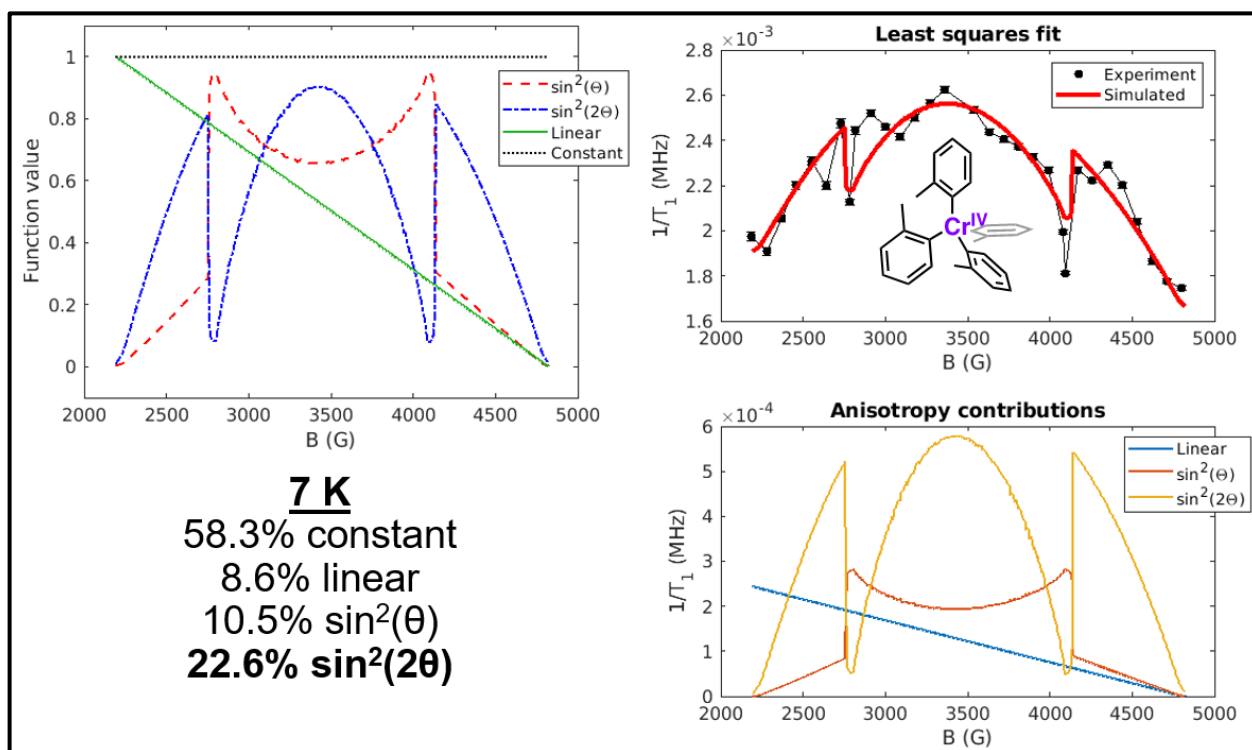


**Figure S18.** Experimental and simulated  $T_1$  anisotropy plots for 1.8%  $\text{Cr}(o\text{-tolyl})_4$  in  $\text{Sn}(o\text{-tolyl})_4$  at 7 K. The  $\sin^2(2\theta)$  form dominates the fit.

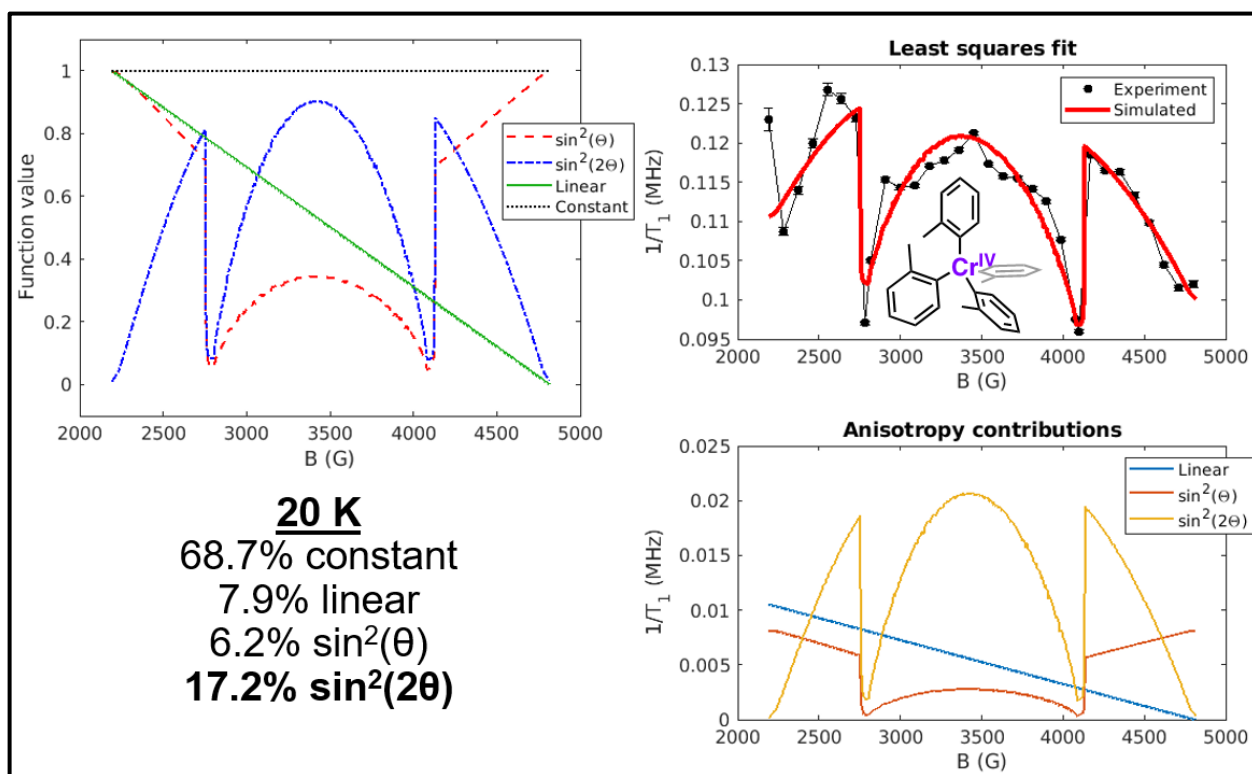


**Figure S19.** Experimental and simulated  $T_1$  anisotropy plots for 1.8% Cr(*o*-tolyl)<sub>4</sub> in Sn(*o*-tolyl)<sub>4</sub> at 20 K. The  $\sin^2(2\theta)$  form dominates the fit.

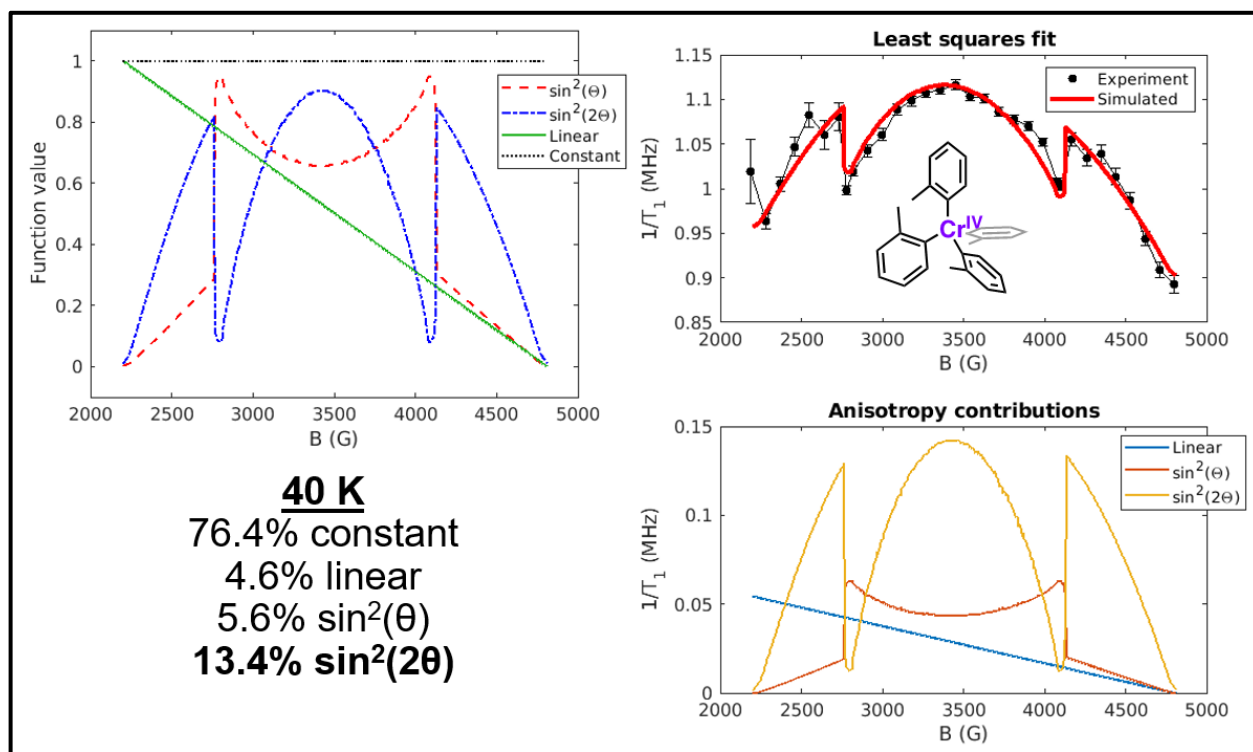


**Figure S20.** Experimental and simulated  $T_1$  anisotropy plots for 1.8% Cr(*o*-tolyl)<sub>4</sub> in Sn(*o*-tolyl)<sub>4</sub> at 40 K. The  $\sin^2(2\theta)$  form dominates the fit.

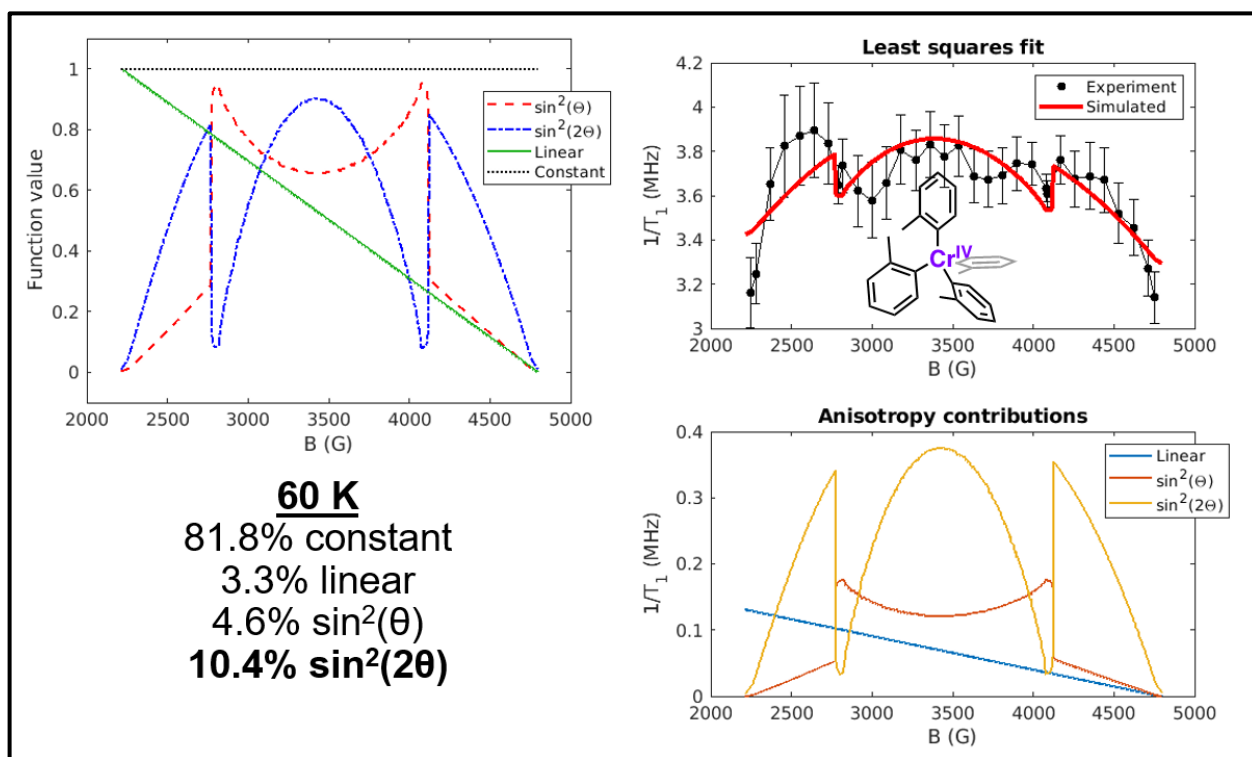


**Figure S21.** Experimental and simulated  $T_1$  anisotropy plots for 1.8%  $\text{Cr}(\text{o-tolyl})_4$  in  $\text{Sn}(\text{o-tolyl})_4$  at 60 K. The  $\sin^2(2\theta)$  form dominates the fit.

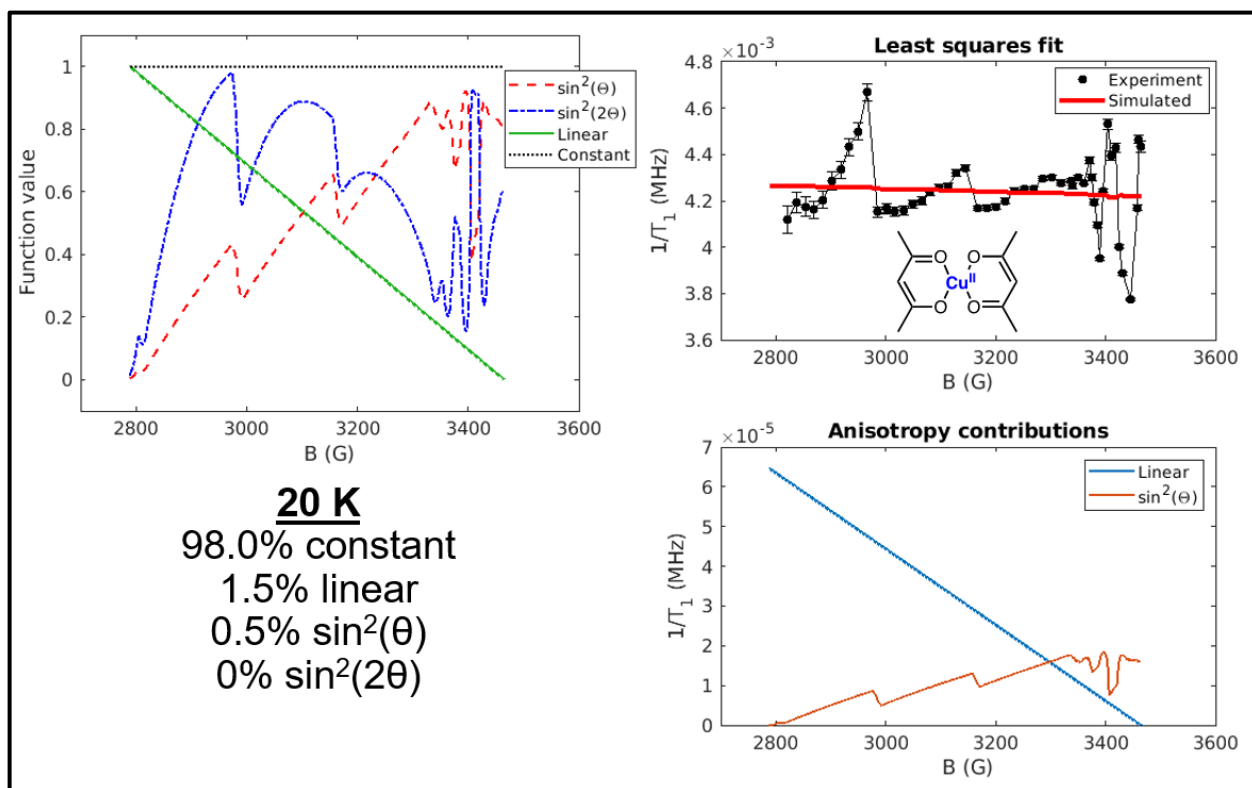




**Figure S22.** Experimental and simulated  $T_1$  anisotropy plots for 0.1% Cu(acac)<sub>2</sub> in Pd(acac)<sub>2</sub> at 20 K. Inclusion of the  $\sin^2(2\theta)$  functions worsened the fit, and thus this contribution was set to 0%. The data show virtually no  $T_1$  anisotropy that can be fit by the given predictor functions.

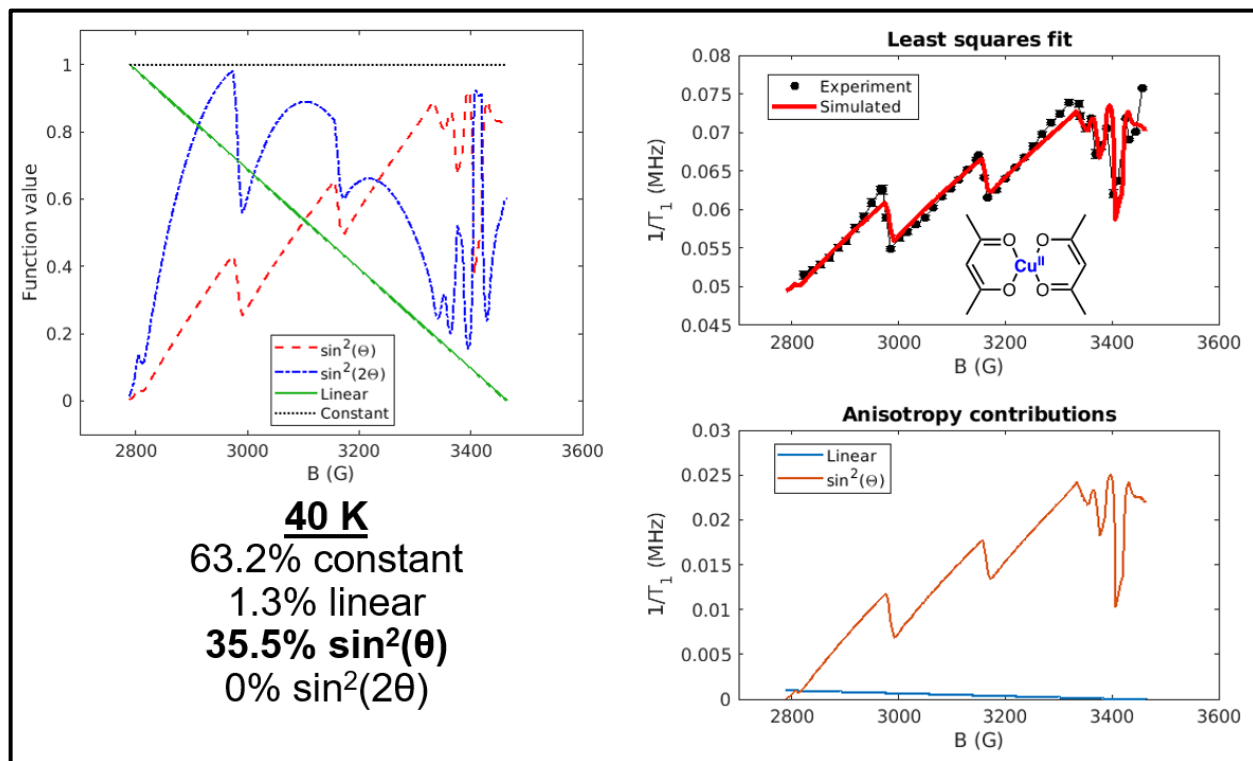


**Figure S23.** Experimental and simulated  $T_1$  anisotropy plots for 0.1% Cu(acac)<sub>2</sub> in Pd(acac)<sub>2</sub> at 40 K. Inclusion of the  $\sin^2(2\theta)$  functions worsened the fit, and thus this contribution was set to 0%. The  $\sin^2(\theta)$  form dominates the fit.

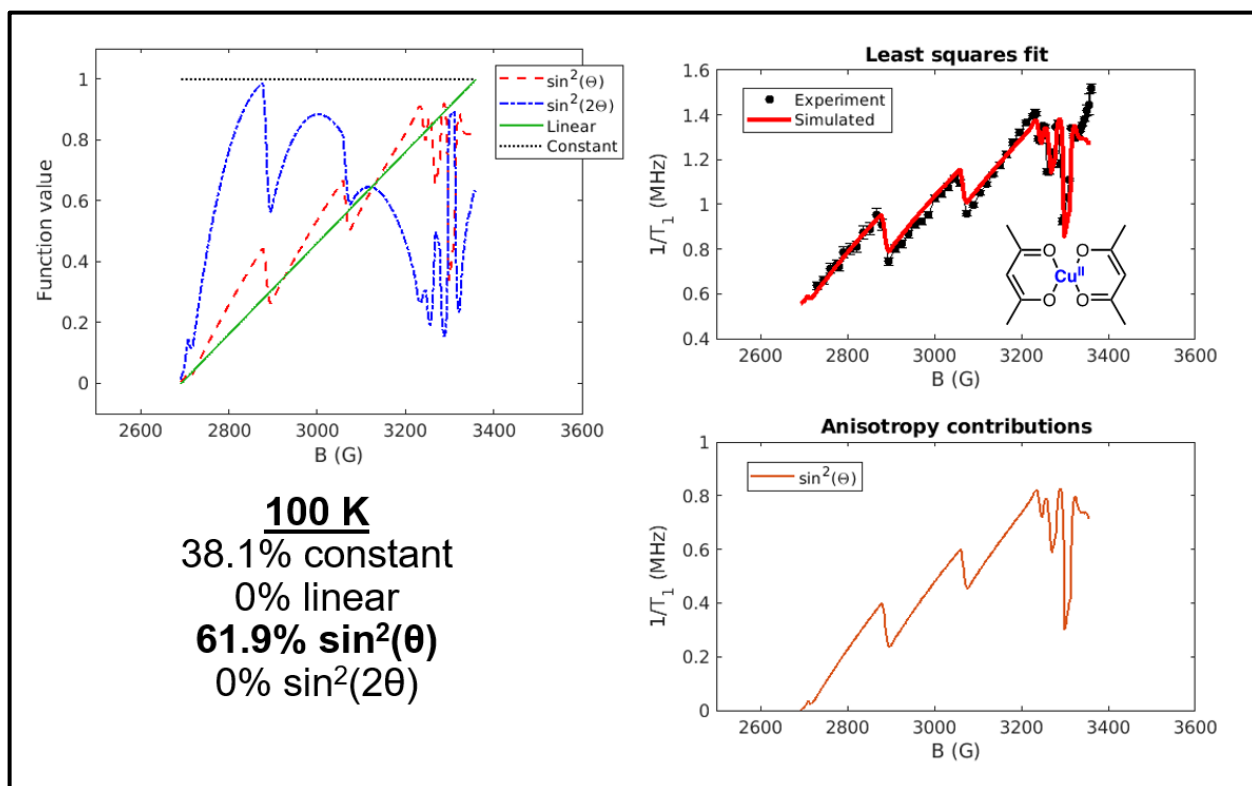


**Figure S24.** Experimental and simulated  $T_1$  anisotropy plots for 0.1%  $\text{Cu}(\text{acac})_2$  in  $\text{Pd}(\text{acac})_2$  at 100 K. Inclusion of the linear and  $\sin^2(2\theta)$  functions worsened the fit, and, thus, these contributions were set to 0%. The  $\sin^2(\theta)$  form dominates the fit.

**Table S1:** Tabulation of regression coefficients for  $T_1$  anisotropy (absolute magnitudes). Dominant anisotropy contributions are bolded.

Molecule	Temperature (K)	Constant (MHz)	Linear (MHz)	$\sin^2(\theta)$ (MHz)	$\sin^2(2\theta)$ (MHz)
$\text{Cr}(o\text{-tolyl})_4$	7	$1.66 \times 10^{-3}$	$-2.45 \times 10^{-4}$	$2.97 \times 10^{-4}$	<b><math>6.41 \times 10^{-4}</math></b>
	20	$9.17 \times 10^{-2}$	$-1.06 \times 10^{-2}$	$-8.21 \times 10^{-3}$	<b><math>2.29 \times 10^{-2}</math></b>
	40	$9.01 \times 10^{-1}$	$-5.46 \times 10^{-2}$	$6.66 \times 10^{-2}$	<b><math>1.58 \times 10^{-1}</math></b>
	60	$3.29 \times 10^0$	$-1.32 \times 10^{-1}$	$1.86 \times 10^{-1}$	<b><math>4.16 \times 10^0</math></b>
$\text{Cu}(\text{acac})_2$	20	$4.20 \times 10^{-3}$	$-6.46 \times 10^{-5}$	$1.99 \times 10^{-5}$	0
	40	$4.84 \times 10^{-2}$	$-1.03 \times 10^{-3}$	<b><math>2.71 \times 10^{-2}</math></b>	0
	100	$5.55 \times 10^{-1}$	0	<b><math>9.00 \times 10^{-1}</math></b>	0

**Table S2:** Tabulation of regression coefficients for  $T_1$  anisotropy (percentages). Dominant anisotropy contributions are bolded.

Molecule	Temperature (K)	Constant (%)	Linear (%)	$\sin^2(\theta)$ (%)	$\sin^2(2\theta)$ (%)
$\text{Cr}(o\text{-tolyl})_4$	7	58.3	8.6	10.5	<b>22.6</b>
	20	68.7	7.9	6.2	<b>17.2</b>
	40	76.4	4.6	5.6	<b>13.4</b>
	60	81.8	3.3	4.6	<b>10.4</b>

Cu(acac) <sub>2</sub>	20	98.0	1.5	0.5	0
	40	63.2	1.3	<b>35.5</b>	0
	100	38.1	0	<b>61.9</b>	0

In this work, we refer to the key features of the  $1/T_1$  plots as “ $\sin^2(\theta)$ ” or “ $\sin^2(2\theta)$ ” anisotropy functions, but it is frequently the case that the majority of the relaxation rate is isotropic (as in the fitting contributions in **Figure S17**). This does not negate the utility of studying  $T_1$  anisotropy, which provides a means to identify distinct contributions to the spin relaxation regardless of how large the isotropic component is. It does mean, however, that care must be taken when mapping observed  $T_1$  anisotropy behavior onto individual vibrational modes. Any given phonon may contribute to relaxation along all orientations but do so unequally – such a phonon will contribute *both* to the isotropic and anisotropic components of the  $T_1$  (**Figure S17**).

Consider a hypothetical case where the relaxation rate is about 66% isotropic and 33% anisotropic (e.g.  $\sin^2(\theta)$ ). This is entirely consistent with two distinct scenarios of vibrational origin. (a) There exists a single vibrational mode which has 100% of the thermal population, and induces parallel relaxation with relative rate 1 and perpendicular relaxation with relative rate 3/2. The common rate of 1 shared across all orientations contributes to the isotropic component of  $1/T_1$ , while the  $\frac{1}{2}$  that is in excess at the perpendicular orientation defines the anisotropic contribution. (b) There exist two vibrational modes I and II. Mode I has 66% of the thermal population and contributes an identical relative rate 1 across all orientations, while mode II has 33% of the thermal population and contributes  $\frac{1}{2}$  to the perpendicular rate while not contributing at all to parallel orientation relaxation. The  $T_1$  anisotropy observed is identical in both cases. However, if modes I and II have distinct energies in case (b), a variable temperature  $T_1$  anisotropy study such as shown in **Figure 3** will be able to alter the thermal populations, decreasing or increasing the anisotropy with temperature. In case (a), the  $T_1$  anisotropy will not change with temperature unless other vibrational modes become thermally populated. Temperature-dependent  $T_1$  anisotropy studies are thus a powerful tool for assigning the physical origins of the observed relaxation rates.

## 6. Theoretical Derivation of $T_1$ Anisotropy Functional Forms

### 6.1 $S = \frac{1}{2}$ rotational mode $T_1$ anisotropy

The connection between rotational motion and trigonometric functional forms was developed by Eaton & Eaton in the context of  $S = \frac{1}{2}$   $T_m$  anisotropy.<sup>14,15</sup> To derive the  $\sin^2(2\theta)$  functional form for impact of rotational modes on  $T_1$  instead, we will first start with the spin Hamiltonian model for  $S = \frac{1}{2}$  spin-phonon coupling, which is appropriate for  $\text{Cu}(\text{acac})_2$ . We will then show how this concept generalizes to the  $S = 1$  case appropriate for the  $\text{Cr}(o\text{-tolyl})_4$  and leads to the identical  $\sin^2(2\theta)$  functional form.

As used in this discussion, a “rotational mode” is any molecular motion which causes rotation of principal tensor axes of the magnetic Hamiltonian. For example, if an  $S = \frac{1}{2}$  molecule is initially aligned so that the magnetic field is oriented along  $g_z$ , molecular movement along the rotational mode may cause the magnetic field to lose alignment with  $g_z$  and become partially aligned with  $g_x$  or  $g_y$ . This does not necessarily imply that the mode under consideration is a rigid-body molecular rotation (i.e., one of the degrees of freedom not included in 3N-6 vibrational modes). Instead, the first coordination sphere could rotate along, say, the molecular y axis, while the ligand framework rotates in the opposite direction – this motion ubiquitously occurs in vibrational modes of symmetry  $e_g$  for square planar ( $D_{4h}$ ) molecules with extended ligand structures, such as copper phthalocyanine.<sup>16,17</sup> Alternatively, a rotational mode could arise from acoustic phonons, pseudo-acoustic phonons, or librations (the latter in a disordered or glassy environment). Since the g-tensor is primarily sensitive to the motion of the first coordination sphere, these five options (true rotation,  $e_g$  vibrational mode, acoustic phonon, pseudo-acoustic phonon, and glassy libration) could all cause the magnetic tensor axes to rotate in a similar way. EPR can only probe the motion of the magnetic tensor axes, meaning these motions could lead to similar  $T_1$  anisotropy patterns. Nonetheless, we are able to use the temperature dependence of the anisotropy to rule out higher energy ( $> 50 \text{ cm}^{-1}$ ) molecular  $e_g$  symmetry vibrations (see **Figure 3**, main text).

Many contemporary spin-phonon coupling models for molecular qubits have invoked the quantity  $\partial g / \partial Q$  as the key coefficient describing how a vibrational mode induces spin relaxation.<sup>16–18</sup> While recent work on  $T_1$  anisotropy has shown that  $\partial g / \partial Q$  is properly understood as a proxy for the true physical mechanism involving vibrational mixing of minority spin wavefunction components,<sup>5</sup> here calculation of  $\partial g / \partial Q$  is sufficient to account for the observed  $T_1$  anisotropy, and, thus, we employ this simplified model. Proceeding with the above understanding of a rotational mode, the mode coordinate  $Q$  is equivalent to the rotation angle  $\theta$  that mixes  $g_z$  into  $g_x$  or  $g_y$ . We therefore want to calculate  $\partial g / \partial \theta$  as the spin-phonon coupling coefficient, which is a proxy for the spin-flip matrix element. By analogy to Fermi’s golden rule, the squared matrix element  $(\partial g / \partial \theta)^2$  is proportional to the average transition rate, so we expect  $1/T_1 \propto (\partial g / \partial \theta)^2$ .

We can compute the derivative of the measured g value along any orientation,  $(\partial g / \partial \theta)^2$  by leveraging the standard EPR equation for how the g value changes with the orientation of the molecule in axial symmetry:

$$g^2(\theta) = g_{\parallel}^2 \cos^2 \theta + g_{\perp}^2 \sin^2 \theta \quad (\text{S3})$$

$$g(\theta) = \sqrt{g_{\parallel}^2 \cos^2 \theta + g_{\perp}^2 \sin^2 \theta} \quad (\text{S4})$$

Making the following simplifying definition,

$$\Delta g^2 = g_{\parallel}^2 - g_{\perp}^2 \quad (\text{S5})$$

We obtain:

$$g(\theta) = \sqrt{\Delta g^2 \cos^2 \theta + g_{\perp}^2} \quad (\text{S6})$$

Differentiation with respect to  $\theta$  then yields:

$$\frac{\partial g}{\partial \theta} = \frac{(\Delta g^2) \sin 2\theta}{2\sqrt{\Delta g^2 \cos^2 \theta + g_{\perp}^2}} \quad (\text{S7})$$

Since the g anisotropy is small relative to the total g value, we can write:

$$\sqrt{\Delta g^2 \cos^2 \theta + g_{\perp}^2} \approx g_{\perp} \quad (\text{S8})$$

Which yields the simplification:

$$\frac{\partial g}{\partial \theta} = \left( \frac{\Delta g^2}{2g_{\perp}} \sin 2\theta \right) \quad (\text{S9})$$

The spin relaxation rate is given by squaring this matrix element proxy:

$$\frac{1}{T_1} \propto \left( \frac{\partial g}{\partial \theta} \right)^2 \propto \sin^2(2\theta) \quad (\text{S10})$$

This shows that the  $T_1$  anisotropy induced by a rotational mode in an  $S = 1/2$  complex with axial g-tensor anisotropy should follow the  $\sin^2(2\theta)$  functional form.

## 6.2 $S = 1$ rotational mode $T_1$ anisotropy

In  $S = 1$   $\text{Cr}(o\text{-tolyl})_4$ , the dominant magnetic anisotropy arises from the axial zero-field splitting tensor (parameterized as  $D$ ) rather than the g-tensor. Unlike g,  $D$  is generally taken as a constant for the molecule, but it anisotropically affects the energy levels and resonant field positions for different molecular orientations. The correct analogy to the preceding  $S = 1/2$   $\partial g / \partial \theta$  derivation is therefore to calculate  $\partial B_{res} / \partial \theta$ . Indeed, this formulation was originally employed by Eaton & Eaton for  $S = 1/2$  systems as well.<sup>14</sup>

At X-band, the Zeeman splitting is  $> 0.3 \text{ cm}^{-1}$ , while  $D$  is only  $\sim 0.1 \text{ cm}^{-1}$  in  $\text{Cr}(\text{aryl})_4$  qubits. Therefore, it is appropriate to take the Zeeman interaction as the zeroth-order Hamiltonian and treat  $D$  as a perturbation. Examination of the energy level diagrams in **Figures S5-S6** supports this conclusion. Additionally, we take the magnetic field as the z-axis for quantization of the  $M_s$  levels

and rotate the zero-field splitting Hamiltonian to coincide with this choice of axes. The Zeeman Hamiltonian is thus given by:

$$H_{Zeeman} = gB\hat{S}_z \quad (\text{S11})$$

In its principal tensor axes frame, the axial zero field splitting Hamiltonian is given by:

$$H_{ZFS} = \vec{S} \cdot \mathbf{D} \cdot \vec{S} = \begin{pmatrix} \hat{S}_x & \hat{S}_y & \hat{S}_z \end{pmatrix} \begin{pmatrix} -\frac{D}{3} & 0 & 0 \\ 0 & -\frac{D}{3} & 0 \\ 0 & 0 & \frac{2D}{3} \end{pmatrix} \begin{pmatrix} \hat{S}_x \\ \hat{S}_y \\ \hat{S}_z \end{pmatrix} \quad (\text{S12})$$

However, this Hamiltonian is not in the same basis as the Zeeman Hamiltonian whenever the magnetic field is applied at an angle  $\theta \neq 0$  to the z-axis of the zero-field splitting Hamiltonian. In this case, we must rotate the ZFS tensor to have the same axes as the g-tensor, which we accomplish via tensor rotations:

$$\begin{aligned} \mathbf{D}(\theta) &= \begin{pmatrix} \cos(\theta) & 0 & \sin(\theta) \\ 0 & 1 & 0 \\ -\sin(\theta) & 0 & \cos(\theta) \end{pmatrix} \begin{pmatrix} -\frac{D}{3} & 0 & 0 \\ 0 & -\frac{D}{3} & 0 \\ 0 & 0 & \frac{2D}{3} \end{pmatrix} \begin{pmatrix} \cos(\theta) & 0 & -\sin(\theta) \\ 0 & 1 & 0 \\ \sin(\theta) & 0 & \cos(\theta) \end{pmatrix} \\ &= \begin{pmatrix} \frac{D}{3}(3\sin^2\theta - 1) & 0 & \frac{D}{2}\sin(2\theta) \\ 0 & -\frac{D}{3} & 0 \\ \frac{D}{2}\sin(2\theta) & 0 & \frac{D}{3}(3\cos^2\theta - 1) \end{pmatrix} \end{aligned} \quad (\text{S13})$$

So the ZFS Hamiltonian of the molecule with magnetic field rotated by an angle  $\theta$  to the ZFS z-axis is given by:

$$\begin{aligned} H_{ZFS}(\theta) &= \vec{S} \cdot \mathbf{D}(\theta) \cdot \vec{S} \\ &= \frac{D}{3}(3\sin^2\theta - 1)\hat{S}_x^2 - \frac{D}{3}\hat{S}_y^2 + \frac{D}{3}(3\cos^2\theta - 1)\hat{S}_z^2 \\ &\quad + \frac{D}{2}\sin(2\theta)[\hat{S}_z\hat{S}_x + \hat{S}_x\hat{S}_z] \end{aligned} \quad (\text{S14})$$

Application of first order perturbation theory tells us the energies are given by

$$E_{ZFS}(M_s) = B\beta g M_s + \langle M_s | H_{ZFS} | M_s \rangle \quad (\text{S15})$$

We can compute the matrix elements on the right-hand side of **Equation S15** directly from **Equation S14**:

$$\langle -1 | H_1 | -1 \rangle = \frac{D}{6}(3\cos^2\theta - 1) \quad (\text{S16})$$

$$\langle 0 | H_1 | 0 \rangle = -\frac{D}{3}(3\cos^2\theta - 1) \quad (\text{S17})$$

Now, considering the ground state transition between  $M_s = -1 \rightarrow M_s = 0$ , we have the energy gap:

$$E(M_s = 0) - E(M_s = -1) = \Delta E = B\beta g - \frac{D}{2}(3\cos^2\theta - 1) \quad (\text{S18})$$

The derivative of the ground state transition energy goes as  $\sin(2\theta)$ :

$$\frac{\partial \Delta E}{\partial \theta} = \frac{3D}{2} \sin(2\theta) \quad (\text{S19})$$

This has been obtained for the ground state  $M_s = -1 \rightarrow M_s = 0$  transition, but by symmetry, the same  $\theta$  dependence will hold for  $M_s = 0 \rightarrow M_s = +1$ . The resonant field is directly proportional to the zero-field splitting, which is the only term with an angular dependence in the spin Hamiltonian for isotropic g:

$$B_{res}(\theta) = \frac{h\nu}{\beta g} + \frac{D}{2\beta g} (3 \cos^2 \theta - 1) \quad (\text{S20})$$

Thus, the derivative of the resonant field also goes as  $\sin(2\theta)$ :

$$\frac{\partial B_{res}}{\partial \theta} = -\frac{3D}{2\beta g} \sin(2\theta) \quad (\text{S21})$$

In the  $S = 1/2$  derivation, the term  $\partial g / \partial \theta$  also controls the modulation of the resonant field with vibrational motion. For the  $S = 1$  case with multiple Hamiltonian terms, the spin flip matrix element is approximated proportional to the modulation of the resonant field by the rotational mode:

$$\frac{1}{T_1} \propto \left| \frac{\partial B_{res}}{\partial \theta} \right|^2 \propto \sin^2(2\theta) \quad (\text{S22})$$

This shows that  $1/T_1 \propto \sin^2(2\theta)$  for rotational modes in both the  $S = 1$  and  $S = 1/2$  cases considered.

## 7. Tabulated $T_1$ Values

**Table S3.**  $T_1$  values extracted from stretched exponential fits of inversion recovery data at various fields and temperatures for a 1.8% Cr(*o*-tolyl)<sub>4</sub> in Sn(*o*-tolyl)<sub>4</sub> sample at X-band,  $\pi = 16$  ns pulses.

Field (G)	$T_1$ Extracted from Stretched Exponential Fits ( $\mu$ s)			
	7 K	20 K	40 K	60 K
2190	506.8	8.126	0.981	-
2245	-	-	-	0.316
2280	524.2	9.199	1.038	0.308
2370	487.0	8.774	0.994	0.273
2460	454.5	8.336	0.955	0.261
2550	433.3	7.888	0.923	0.258
2640	454.7	7.958	0.942	0.256
2730	403.7	8.119	0.925	0.260
2781	470.2	10.30	1.001	0.274
2820	409.0	9.524	0.980	0.267
2910	397.0	8.675	0.959	0.276
3000	406.7	8.747	0.942	0.279
3090	414.1	8.730	0.918	0.273
3180	400.1	8.538	0.910	0.262
3270	390.3	8.490	0.902	0.265
3360	381.1	8.394	0.899	0.260
3420	300.3	6.589	0.757	0.216
3450	351.2	8.252	0.895	0.264
3540	394.8	8.521	0.905	0.261
3630	410.5	8.640	0.908	0.271
3720	416.0	8.655	0.920	0.272
3810	421.3	8.753	0.927	0.271
3900	429.5	8.883	0.934	0.267
3990	440.9	9.285	0.950	0.267
4080	501.5	10.25	0.992	0.275
4084	-	-	-	0.277
4097	552.1	10.42	0.998	-
4170	441.0	8.435	0.947	0.265
4260	450.1	8.587	0.966	0.272
4350	436.7	8.600	0.962	0.271
4440	454.5	8.820	0.986	0.272
4530	490.2	9.105	1.013	0.284
4620	536.8	9.574	1.059	0.289
4710	563.0	9.848	1.099	0.305
4755	-	-	-	0.318
4800	572.3	9.806	1.120	-



**Table S4.**  $T_1$  values extracted from stretched exponential fits of inversion recovery data at various fields and temperatures for a 0.1% Cu(acac)<sub>2</sub> in Pd(acac)<sub>2</sub> sample at X-band,  $\pi = 16$  ns pulses. 20 K and 40 K experiments conducted at 9.727 GHz, while 100 K experiment conducted at 9.418 GHz.

Field (G)	$T_1$ Extracted from Stretched Exponential Fits ( $\mu$ s)		Field (G)	$T_1$ Extracted from Stretched Exponential Fits ( $\mu$ s)
	20 K	40 K		100 K
2822	242.7	19.41	2730	1.570
2838	238.6	19.19	2745	1.512
2854	239.5	18.90	2760	1.400
2870	240.3	18.62	2775	1.367
2886	237.9	18.16	2780	1.381
2902	233.4	17.90	2790	1.272
2918	230.8	17.35	2805	1.249
2934	225.6	16.94	2820	1.232
2950	222.3	16.43	2835	1.145
2966	214.2	15.99	2850	1.122
2970	-	15.99	2865	1.050
2977	-	16.96	2880	1.102
2985	240.9	18.21	2895	1.343
3001	239.9	17.76	2910	1.248
3017	240.0	17.53	2925	1.214
3033	240.7	17.23	2940	1.153
3049	240.5	16.95	2955	1.099
3065	238.8	16.58	2970	1.081
3081	238.1	16.22	2985	1.048
3097	236.1	15.93	3000	0.974
3113	234.9	15.65	3015	0.955
3129	234.6	15.34	3030	0.927
3145	231.5	15.03	3045	0.898
3150	-	14.93	3060	0.912
3160	-	15.57	3075	1.041
3167	240.0	16.25	3090	1.002
3184	239.8	16.00	3105	0.951
3201	239.6	15.60	3120	0.917
3218	238.2	15.28	3135	0.881
3235	235.7	14.98	3150	0.850
3252	235.2	14.66	3165	0.817
3269	235.2	14.33	3180	0.782
3286	232.9	14.02	3195	0.756
3303	232.5	13.80	3210	0.733
3320	233.7	13.53	3225	0.716
3337	233.3	13.56	3230	0.708
3340	234.5	13.86	3235	0.711

3350	232.5	14.16	3240	0.772
3360	233.8	13.93	3245	0.779
3370	228.5	14.87	3250	0.740
3375	232.4	14.64	3255	0.741
3380	238.5	19.41	3260	0.872
3385	244.2	-	3265	0.872
3390	253.1	14.17	3270	0.850
3395	235.7	-	3275	0.810
3403	220.7	16.11	3280	0.742
3411	227.6	15.68	3285	0.734
3418	225.8	-	3290	0.846
3425	249.9	13.93	3295	1.082
3432	257.3	14.48	3300	1.057
3445	264.9	14.27	3305	0.971
3457	239.8	13.20	3310	0.900
3461	224.0	-	3315	0.744
3465	225.5	-	3320	0.765
			3325	0.770
			3330	0.762
			3335	0.750
			3340	0.737
			3345	0.724
			3350	0.705
			3355	0.691
			3360	0.658

## References

- (1) Knorr, R.; Lattke, E.; Rapple, E. Der Konformative *Ortho* -Effekt Bei *o* -Tolylstilbenen Und Deren Vinylithiumderivaten. *Chem. Ber.* **1981**, *114* (5), 1581–1591. <https://doi.org/10.1002/cber.19811140502>.
- (2) Koschmieder, S. U.; McGilligan, B. S.; McDermott, G.; Arnold, J.; Wilkinson, G.; Hussain-Bates, B.; Hursthouse, M. B. Aryl and Aryne Complexes of Chromium, Molybdenum, and Tungsten. X-Ray Crystal Structures of [Cr(2-MeC<sub>6</sub>H<sub>4</sub>)(μ-2-MeC<sub>6</sub>H<sub>4</sub>)(PMe<sub>3</sub>)<sub>2</sub>]<sub>2</sub>, Mo(η<sup>2</sup>-2-MeC<sub>6</sub>H<sub>3</sub>)(2-MeC<sub>6</sub>H<sub>4</sub>)<sub>2</sub> (PMe<sub>2</sub>Ph)<sub>2</sub>, and W(η<sup>2</sup>-2,5-Me<sub>2</sub>C<sub>6</sub>H<sub>2</sub>)(2,5-Me<sub>2</sub>C<sub>6</sub>H<sub>3</sub>)<sub>2</sub>-(PMe<sub>3</sub>)<sub>2</sub>. *J Chem Soc Dalton Trans* **1990**, No. 11, 3427–3433. <https://doi.org/10.1039/DT9900003427>.
- (3) Bayliss, S. L.; Laorenza, D. W.; Mintun, P. J.; Kovos, B. D.; Freedman, D. E.; Awschalom, D. D. Optically Addressable Molecular Spins for Quantum Information Processing. *Science* **2020**, *370* (6522), 1309–1312. <https://doi.org/10.1126/science.abb9352>.
- (4) Laorenza, D. W.; Kairalapova, A.; Bayliss, S. L.; Goldzak, T.; Greene, S. M.; Weiss, L. R.; Deb, P.; Mintun, P. J.; Collins, K. A.; Awschalom, D. D.; Berkelbach, T. C.; Freedman, D. E. Tunable Cr<sup>4+</sup> Molecular Color Centers. *J. Am. Chem. Soc.* **2021**, *143*, 21350–21363. <https://doi.org/10.1021/jacs.1c10145>.
- (5) Kazmierczak, N. P.; Hadt, R. G. Illuminating Ligand Field Contributions to Molecular Qubit Spin Relaxation via *T*<sub>1</sub> Anisotropy. *J. Am. Chem. Soc.* **2022**, *144* (45), 20804–20814. <https://doi.org/10.1021/jacs.2c08729>.
- (6) Stoll, S.; Schweiger, A. EasySpin, a Comprehensive Software Package for Spectral Simulation and Analysis in EPR. *J. Magn. Reson.* **2006**, *178* (1), 42–55. <https://doi.org/10.1016/j.jmr.2005.08.013>.
- (7) Standley, K. J.; Vaughan, R. A. *Electron Spin Relaxation Phenomena in Solids*; Springer US: Boston, MA, 1969. <https://doi.org/10.1007/978-1-4899-6539-4>.
- (8) Mowat, W.; Shortland, A. J.; Hill, N. J.; Wilkinson, G. Elimination Stabilized Alkyls. Part II. Neopentyl and Related Alkyls of Chromium(IV). *J. Chem. Soc. Dalton Trans.* **1973**, No. 7, 770. <https://doi.org/10.1039/dt9730000770>.
- (9) Myers, B. A.; Ariyaratne, A.; Jayich, A. C. B. Double-Quantum Spin-Relaxation Limits to Coherence of Near-Surface Nitrogen-Vacancy Centers. *Phys. Rev. Lett.* **2017**, *118* (19), 197201. <https://doi.org/10.1103/PhysRevLett.118.197201>.
- (10) Janicka, K.; Wysocki, A. L.; Park, K. Computational Insights into Electronic Excitations, Spin–Orbit Coupling Effects, and Spin Decoherence in Cr(IV)-Based Molecular Qubits. *J. Phys. Chem. A* **2022**, *126* (43), 8007–8020. <https://doi.org/10.1021/acs.jpca.2c06854>.
- (11) Souza-de la Vega, A.; Pandharkar, R.; Strocio, G. D.; Sarkar, A.; Truhlar, D. G.; Gagliardi, L. Multiconfiguration Pair-Density Functional Theory for Chromium(IV) Molecular Qubits. *JACS Au* **2022**, *2* (9), 2029–2037. <https://doi.org/10.1021/jacsau.2c00306>.
- (12) Mirzoyan, R.; Kazmierczak, N. P.; Hadt, R. G. Deconvolving Contributions to Decoherence in Molecular Electron Spin Qubits: A Dynamic Ligand Field Approach. *Chem. – Eur. J.* **2021**, *27*, 9482–9494. <https://doi.org/10.1002/chem.202100845>.
- (13) Eaton, S. S.; Eaton, G. R. Multifrequency Pulsed EPR and the Characterization of Molecular Dynamics. In *Methods in Enzymology*; Elsevier, 2015; Vol. 563, pp 37–58. <https://doi.org/10.1016/bs.mie.2015.06.028>.
- (14) Du, J.-L.; More, K. M.; Eaton, S. S.; Eaton, G. R. Orientation Dependence of Electron Spin Phase Memory Relaxation Times in Copper(II) and Vanadyl Complexes in Frozen Solution. *Isr. J. Chem.* **1992**, *32* (2–3), 351–355. <https://doi.org/10.1002/ijch.199200041>.

- (15) Eaton, S. S.; Eaton, G. R. Relaxation Mechanisms. In *eMagRes*; Wiley, 2016; pp 1543–1556. <https://doi.org/10.1002/9780470034590.emrstm1507>.
- (16) Kazmierczak, N. P.; Mirzoyan, R.; Hadt, R. G. The Impact of Ligand Field Symmetry on Molecular Qubit Coherence. *J. Am. Chem. Soc.* **2021**, *143* (42), 17305–17315. <https://doi.org/10.1021/jacs.1c04605>.
- (17) Santanni, F.; Albino, A.; Atzori, M.; Ranieri, D.; Salvadori, E.; Chiesa, M.; Lunghi, A.; Bencini, A.; Sorace, L.; Totti, F.; Sessoli, R. Probing Vibrational Symmetry Effects and Nuclear Spin Economy Principles in Molecular Spin Qubits. *Inorg. Chem.* **2021**, *60* (1), 140–151. <https://doi.org/10.1021/acs.inorgchem.0c02573>.
- (18) Lunghi, A.; Sanvito, S. How Do Phonons Relax Molecular Spins? *Sci. Adv.* **2019**, *5* (9), eaax7163. <https://doi.org/10.1126/sciadv.aax7163>.